

<https://helda.helsinki.fi>

---

## Sulfide Minerals as Potential Tracers of Isochemical Processes in Contact Metamorphism: Case Study of the Kochumdek Aureole, East Siberia

Sokol, Ella V.

Multidisciplinary Digital Publishing Institute  
2020-12-25

---

Sokol, E.V.; Deviatiiarova, A.S.; Kokh, S.N.; Reutsky, V.N.; Abersteiner, A.; Philippova, K.A.; Artemyev, D.A. Sulfide Minerals as Potential Tracers of Isochemical Processes in Contact Metamorphism: Case Study of the Kochumdek Aureole, East Siberia. *Minerals* 2020, 11, 17.

---

<http://hdl.handle.net/10138/348909>

---

*Downloaded from Helda, University of Helsinki institutional repository.*


*This is an electronic reprint of the original article.*

*This reprint may differ from the original in pagination and typographic detail.*

*Please cite the original version.*

## Article

# Sulfide Minerals as Potential Tracers of Isochemical Processes in Contact Metamorphism: Case Study of the Kochumdek Aureole, East Siberia

Ella V. Sokol<sup>1</sup>, Anna S. Deviatiiarova<sup>1,\*</sup>, Svetlana N. Kokh<sup>1</sup>, Vadim N. Reutsky<sup>1</sup> , Adam Abersteiner<sup>2,3,4</sup>, Kseniya A. Philippova<sup>5</sup> and Dmitry A. Artemyev<sup>5,6</sup>

- <sup>1</sup> V.S. Sobolev Institute of Geology and Mineralogy, Siberian Branch of the Russian Academy of Sciences, 3 Koptuyug Avenue, 630090 Novosibirsk, Russia; sokol@igm.nsc.ru (E.V.S.); s.n.kokh@gmail.com (S.N.K.); reutsky@igm.nsc.ru (V.N.R.)
- <sup>2</sup> Department of Geosciences and Geography (GeoHel), University of Helsinki, PO Box 64, FIN-00014 Helsinki, Finland; adam.abersteiner@helsinki.fi
- <sup>3</sup> School of Natural Sciences and Centre of Ore Deposits and Earth Sciences (CODES), University of Tasmania, Hobart, Tasmania 7001, Australia
- <sup>4</sup> Institute of Volcanology and Seismology, Far East Branch of the Russian Academy of Sciences, 683006 Petropavlovsk-Kamchatsky, Russia
- <sup>5</sup> South Ural Federal Research Center of Mineralogy and Geoecology, Ural Branch of the Russian Academy of Sciences, Ilmeny Reserve, 456317 Miass, Russia; kseniyafil@yandex.ru (K.A.P.); daartemyev@gmail.com (D.A.A.)
- <sup>6</sup> Geological Department, South Ural State University, 76, Lenin Avenue, 454080 Chelyabinsk, Russia
- \* Correspondence: devyatiiarova@igm.nsc.ru; Tel.: +73-833-302-149



**Citation:** Sokol, E.V.; Deviatiiarova, A.S.; Kokh, S.N.; Reutsky, V.N.; Abersteiner, A.; Philippova, K.A.; Artemyev, D.A. Sulfide Minerals as Potential Tracers of Isochemical Processes in Contact Metamorphism: Case Study of the Kochumdek Aureole, East Siberia. *Minerals* **2021**, *11*, 17. <https://doi.org/10.3390/min11010017>

Received: 23 November 2020

Accepted: 18 December 2020

Published: 25 December 2020

**Publisher's Note:** MDPI stays neutral with regard to jurisdictional claims in published maps and institutional affiliations.



**Copyright:** © 2020 by the authors. Licensee MDPI, Basel, Switzerland. This article is an open access article distributed under the terms and conditions of the Creative Commons Attribution (CC BY) license (<https://creativecommons.org/licenses/by/4.0/>).

**Abstract:** Marly limestones from the Lower Silurian sedimentary units of the Tunguska basin (East Siberia, Russia) underwent metamorphism along the contact with the Early Triassic Kochumdek trap intrusion. At  $\leq 2.5$  m from the contact, the limestones were converted into ultrahigh-temperature marbles composed of pure calcite and sulfide-bearing calcsilicate layers. The sulfide assemblages in the gabbro and marbles were studied as potential tracers of spurrite-merwinite facies alteration. The gabbro-hosted sulfides show Fe-Ni-Cu-Co speciation (pyrrhotite and lesser amounts of chalcopyrite, pentlandite, and cobaltite) and positive  $\delta^{34}\text{S}$  values (+2.7 to +13.1‰). Both matrix and inclusion sulfide assemblages of prograde melilite, spurrite, and merwinite marbles consist dominantly of pyrrhotite and minor amounts of troilite, sphalerite, wurtzite, alabandite, acanthite, and galena. In contrast to its magmatic counterpart, metamorphic pyrrhotite is depleted in Cu (3–2000 times), Ni (7–800 times), Se (20–40 times), Co (12 times), and is isotopically light (about  $-25\%$   $\delta^{34}\text{S}$ ). Broad solid solution series of  $(\text{Zn,Fe,Mn})\text{S}_{\text{cub}}$ ,  $(\text{Zn,Mn,Fe})\text{S}_{\text{hex}}$ , and  $(\text{Mn,Fe})\text{S}_{\text{cub}}$  indicate that the temperature of contact metamorphism exceeded 850–900 °C. No metasomatism or S isotope resetting signatures were detected in the prograde mineral assemblages, but small-scale penetration of magma-derived K- and Cl-rich fluids through more permeable calcsilicate layers was documented based on the distribution of crack-filling Fe-K sulfides (rasvumite, djerfisherite, and bartonite).

**Keywords:** contact metamorphism; marble; pyrrhotite; Fe-K sulfides; Zn-Fe-Mn sulfides; trace elements; sulfur isotope; spurrite-merwinite facies

## 1. Introduction

Petrological analysis of metamorphic rocks commonly aims to reconstruct peak metamorphic conditions and *P-T* paths from data on rock-forming minerals [1–5]. The scope of genetically informative minerals in petrology was improved with the application of the rare earth elements (REE), Ti, and Zr systematics due to the implementation of high-resolution and isotope geochemical analytical techniques [6,7]. The metamorphic conditions of the spurrite-merwinite facies are useful for examining the formation of high-temperature phases that accumulate trace elements [8–10]. Some Ti, U, Zr, Sn, and Sc host phases are

stable across a large range of thermodynamic conditions and can be potential new proxies of metamorphic processes [9,11–15]. Accessory phases are suitable for isotope dating (zircon, monazite) [16], mineral thermometry (Zr-in-rutile, Ti-in-zircon) [17–20] and redox reconstructions (apatite-group minerals, Fe oxides, Fe sulfides, native elements) [5,21–23].

Previously, metamorphic petrologists showed little interest in the mineralogy of sulfides, which re-equilibrate faster than silicates and/or oxides [24], and thus are less likely to record peak metamorphic conditions. Attention to sulfides has been more often focused on their ore potential and the depositional environments of precursor sediments in regional metamorphic complexes [25] or on skarn mineralization in low-grade metamorphic rocks [26]. Meanwhile, sulfide assemblages were recently shown to record changes in metamorphic regimes [27]. Large variations in the major- and trace-element compositions and isotopic  $\delta^{34}\text{S}$  values of sulfides have implications for the source of material involved in the formation of metamorphic-hosted sulfides [28]. Sulfides re-equilibrate and re-crystallize rapidly in response to changes in their growth medium and are thus sensitive to material transport across chemical/geological interfaces. In this respect, sulfides may be independent sources of information on mass transfer between sedimentary and igneous rocks during contact metamorphism [3,8], but to our knowledge have never been used for such purpose.

This idea was tested on the Silurian marly limestones (the Tunguska basin, East Siberia), which was metamorphosed by the Early Triassic Kochumdek gabbro-dolerite sill. According to available data on critical mineral assemblages and numerical simulations [29,30], the Kochumdek aureole results from a single brief thermal event of up to 900 °C and a yearlong peak stage of metamorphism. Therefore, thermal history reconstructions for the Kochumdek area may be relatively simple, more so because it was not subject to any significant later alteration.

This study addresses several issues related to the diverse sulfide mineralization in marbles from the Kochumdek River and in the Kochumdek trap intrusion:

- Major- and trace-element compositions of the marble and gabbro-dolerite samples from the Kochumdek contact aureole;
- Sulfide mineralogy in the marble and gabbro-dolerite samples: diversity, distribution patterns, morphology and age relationships;
- Mineral chemistry of sulfides, including trace-element signatures;
- Sulfur isotope composition.

The goal of the study is to demonstrate that detailed field examination coupled with systematic geochemical analyses of representative rocks and mineralogical studies of sulfides can shed light on the regime of prograde and retrograde igneous-related metamorphism.

## 2. Geological Background

### 2.1. General Information

Diverse sulfide mineralization was reported in the spurrite marbles of the Kochumdek contact aureole [31–35] located in the western termination of the Tunguska basin (the Podkamennaya Tunguska River catchment, East Siberia) [1,2,30,36]. The Tunguska basin is composed of thick sequences (3–7 km in thickness) of Middle Proterozoic to Paleozoic volcano-sedimentary rocks ( $\text{PR}_2\text{--P}_2$ ), which are interbedded with mafic sills and buried under flood basalts over a large part of the basin territory. Continental flood basalt magmatism produced the large igneous province of Siberian Traps at the Permian-Triassic boundary [37–39]. The flood basalts cover an area of ~330,000 km<sup>2</sup> and are localized mainly within the Lower Paleozoic (O-S) strata of the Tunguska basin (Figure 1) [37,40,41].

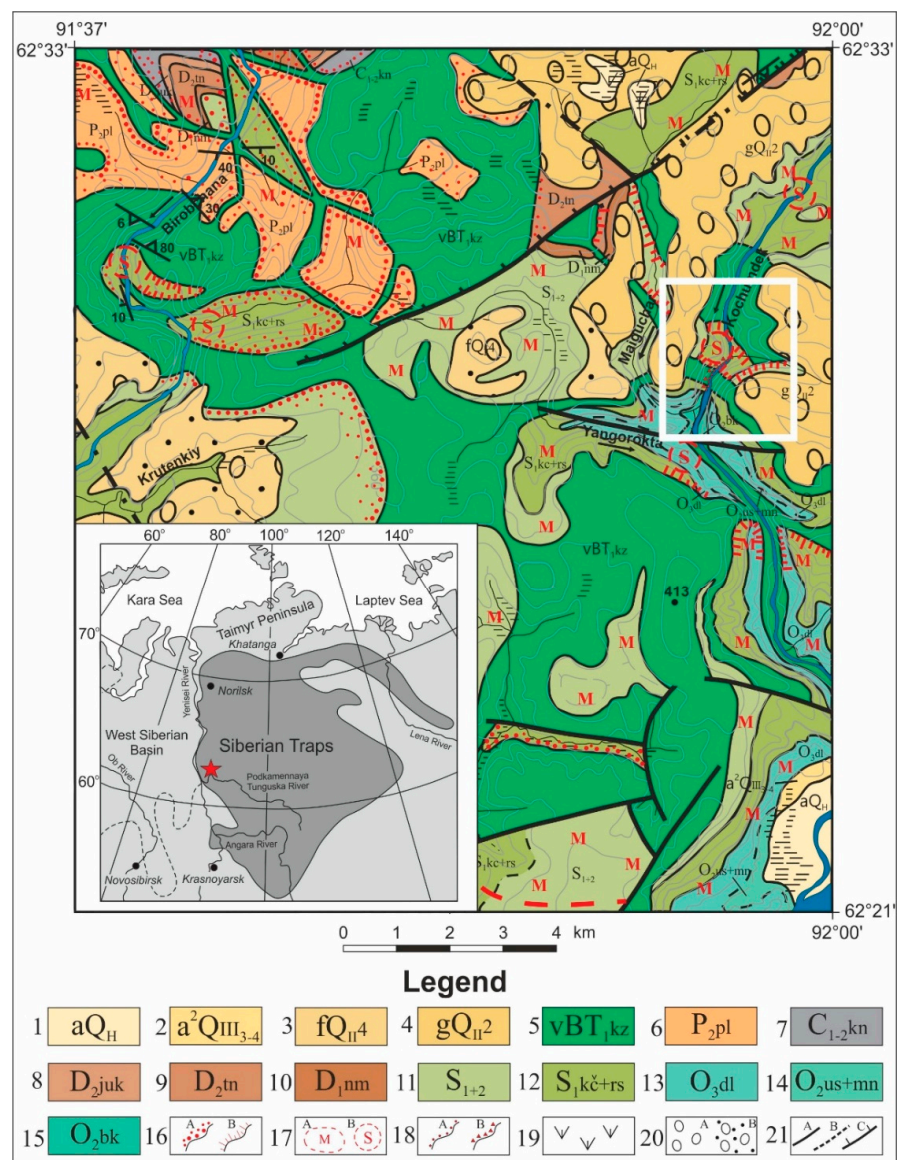


**Figure 1.** Distribution area of the Siberian flood basalt province (Siberian Traps), after [42], and geological map of the study area (red star and white square), modified after the 1:200,000 State Geological Map [43]. Legend corresponds to the 1:1,000,000 State Geological Map [44]. 1–4 = Quaternary sediments (alluvium, fluvioglacial and moraine deposits), 5 = Early Triassic intrusions of the Kuz'movsky complex. Sedimentary strata: 6 = Pelyatkinsk Formation (Permian), 7 = Kondrominsk Formation (Carboniferous), 8 = Yukta Formation (Devonian), 9 = Tynep Formation (Devonian), 10 = Nimsky Formation (Devonian), 11 = Lower and upper parts of the Silurian (combined), 12 = Kochumdek, Kulina, Razvilkinsk Formations of the Lower Silurian (combined), 13 = Dolborska (Ordovician), 14 = Uststolbovaya and Mangazeya Formations united (Ordovician), 15 = Baikit Formation (Ordovician). 16. A = Hornfels, B = Skarny breeds. 17. A = Metasomatic rocks, B = Sulfidation. 18. A = 1981 data, B = 2017 data. Quaternary sediments: 19 = Lake-marsh, 20. A = Water-glacial, B = Glacial. Tectonic contacts: 21. A = Reliable, B = Alleged, C = Reliable, indicating the direction of incidence of the displacer surface.

Early Paleozoic sediments in the Deliga-Kochumdek uplift were intruded by the Early Triassic Kuz'movsky complex (vβT<sub>1,kz</sub>), which exposed the sedimentary rocks and comprises 13% of their area and ≤25% of their volume [44]. The Kuz'movsky complex is comprised of sills that range from 120–300 m in thickness, as well as subordinate dipping bodies and dikes that were emplaced mainly into the horizontally bedded Ordovician and

Silurian mud rock and carbonate sediments. The igneous rocks are mainly of dolerite and gabbro lithologies, and are transitional to gabbro-dolerite, olivine dolerite, and ore-bearing gabbro compositions in the top parts of the intrusions which locally contain pegmatitic lenses and granophyres [29,42–44].

The Tunguska basin is a classical area of contact metamorphism where trap magmatism caused large-scale thermal and/or metasomatic alteration of sediments [1–4,29,45,46]. The interactions of basaltic and sedimentary material produced skarns and calciphyres at the contacts with fluid-saturated differentiated bodies, pyroxene or hornblende hornfels facies along the margins of the poorly differentiated sills [1,2,41,42,44,47] and extremely rare spurrite-merwinite facies (P up to 1.0 kbar and T up to 900 °C) rocks [1,4,29,46].

The Kochumdek aureole of contact metamorphism (Figures 1 and 2) results from the thermal effect of the Kochumdek intrusion (part of the Kuz'movsky complex;  $\nu\beta T_1 kz$ ) on Llandovery ( $S_1ln$ ) marly limestones (Rhuddanian stage, Lower Kochumdek Subformation;  $S_1k\check{c} + rs$ ) [1,2,29,30,36,44,46,47]. Most of the intrusions at the Kochumdek site are gently dipping, poorly differentiated troctolite dolerite sills coexisting with abundant dikes and veins [43,44].

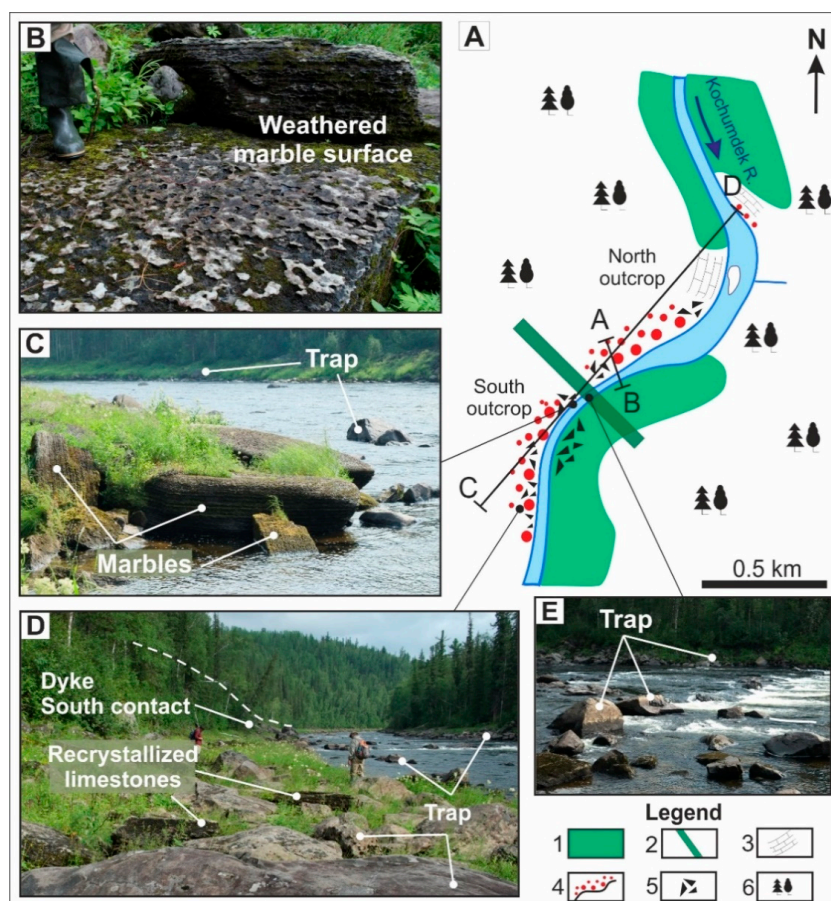


**Figure 2.** Schematic map of sampling site (A) and south outcrop photos (B–E) on the right bank of the Kochumdek River (2017). (B) Weathered marble surface. (C) Scattered blocks of tilleyite and wollastonite marbles. (D) Panoramic photo of right bank of the Kochumdek river floodplain (from south to north). Scattered blocks of recrystallized marly limestones and low-grade marbles from south contact. The rapids in the background of the Kochumdek River consist of gabbro (E). Cross sections along lines A–B and C–D see at Figure 4. 1 = Kochumdek trap, 2 = Dyke, 3 = Recrystallized marly limestones of the Lower Kochumdek Subformation, 4 = Marbles (large and small circles are high- and low-temperature rocks), 5 = Scattered rock blocks, 6 = Taiga.

The 62–64 m thick Lower Kochumdek Subformation ( $S_1k\check{c} + rs$ ) is composed of limestone with thin (0.1–0.5 cm) siltstone or clay intercalations, which contain disseminated pyrite, sphalerite, and galena. The base of the subformation is marked by two beds: (1) dolomitic limestone with layers of bituminous shale, and (2) limestone with rhythmic marl layers [48]. Contact metamorphism within the Kochumdek aureole affected marly limestone with characteristic wavy textures imprinted in marbles (Figure 3A,B,E). The percentage of clay (mainly kaolinite, subordinate illite, and rare smectite) in the sedimentary parent rocks varies from 7% to 47%, while the sand fraction is <1%.

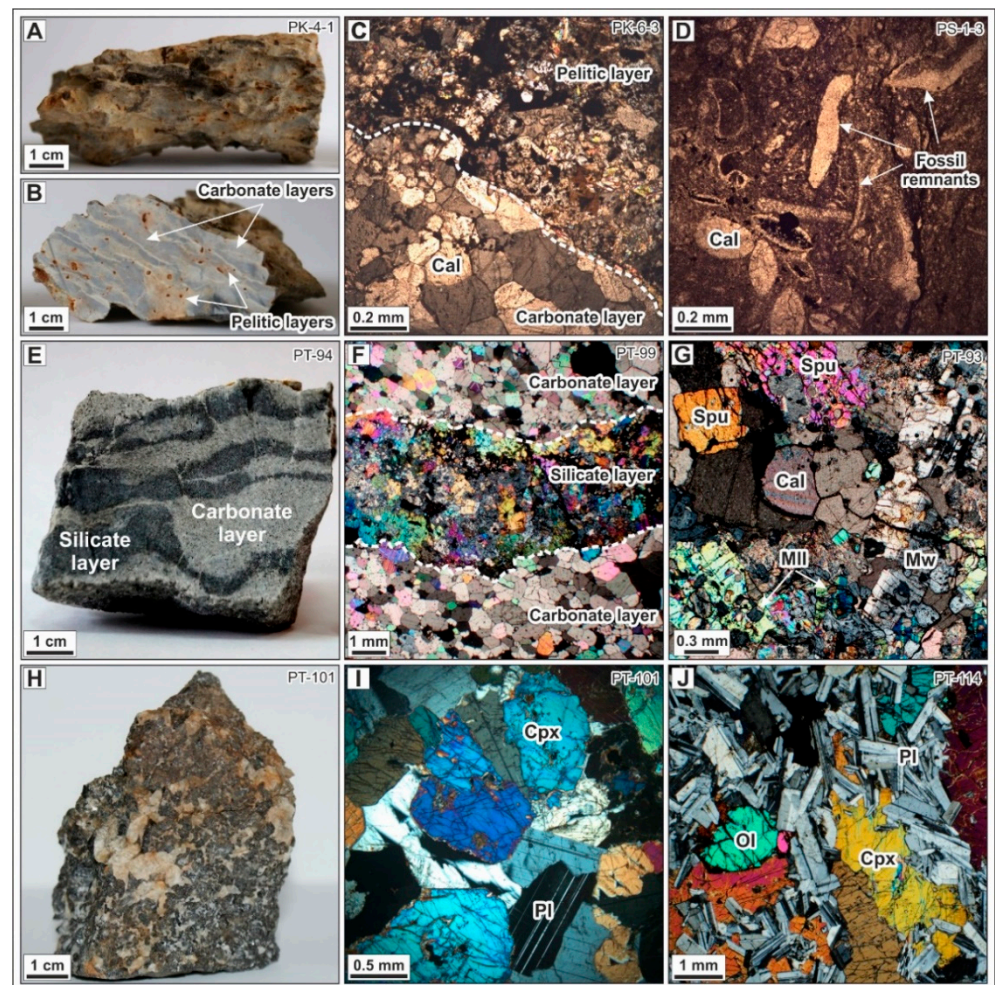


**Figure 3.** Appearance of recrystallized marly limestones (A–D), marbles (E–G) and gabbro (H–J) from the Kochumdek contact aureole. Recrystallized marly limestones: (A) Weathered limestone surface. (B,C) Distribution of carbonate and pelitic layers in limestone. (D) Marly limestone with partially recrystallized fossil remnants. Spurrite marbles: (E) Typical sample of spurrite marble. (F) Silicate and carbonate layers. (G) Calcite + Spurrite + Merwinite + Melilite. Gabbro: (H) Gabbro from the Kochumdek intrusion top. (I,J) Coarse-grained clinopyroxene, with interstitial plagioclase and olivine. (C,D,F,G,I,J) Optical images in cross-polarized transmitted light. Collection: A–D = 2017, E–J = 1981. Cal = calcite, Cpx = clinopyroxene, Mll = melilite, Mtc = monticellite, Mw = merwinite, Ol = olivine, Pl = plagioclase, Spu = spurrite.

## 2.2. Site Description

The sampled contact aureole is located along the right bank of the Kochumdek River (62°27′54.59″ N, 91°55′42.99″ E) at an elevation of 107 m above sea level. This is a permafrost area with a hilly taiga landscape, deeply incised river valleys and flat watersheds that are partly covered by Quaternary glacial deposits (Q<sub>II-III</sub>). Permafrost degradation in the Holocene

post-glacial period produced an erosion cutout till at the top of a sill within 15 km in the lower reaches of the river. An outcrop in the steep river bluffs exposes a continuous sequence of Ordovician pelitic sediments and Llandovery marly limestone intruded by two concordant sills at elevations of 280–320 m and 360–410 m (Figures 1 and 2A).

The largest part of the marble-sill contact is inaccessible, being either submerged below the Kochumdek River level or buried under snow and auffs. High-grade spurrite-merwinite marbles [30] were sampled immediately in the river during a low stand from a horizontal contact between the sill and the overlying carbonate-marl marker bed of the Lower Kochumdek Subformation. Presumed remnants of a large aureole appear on the riverside and on a low right-side terrace above the contact as scattered blocks of tilleyite-wollastonite marble and recrystallized marly limestone (Figure 2A–D), where most of the blocks have horizontal bedding and appear autochthonous (Figure 2B,C). Their origin from an aureole, which was destroyed by postglacial erosion but survived in sags of the upper sill margin, can be inferred from the geological context (Figure 4B).

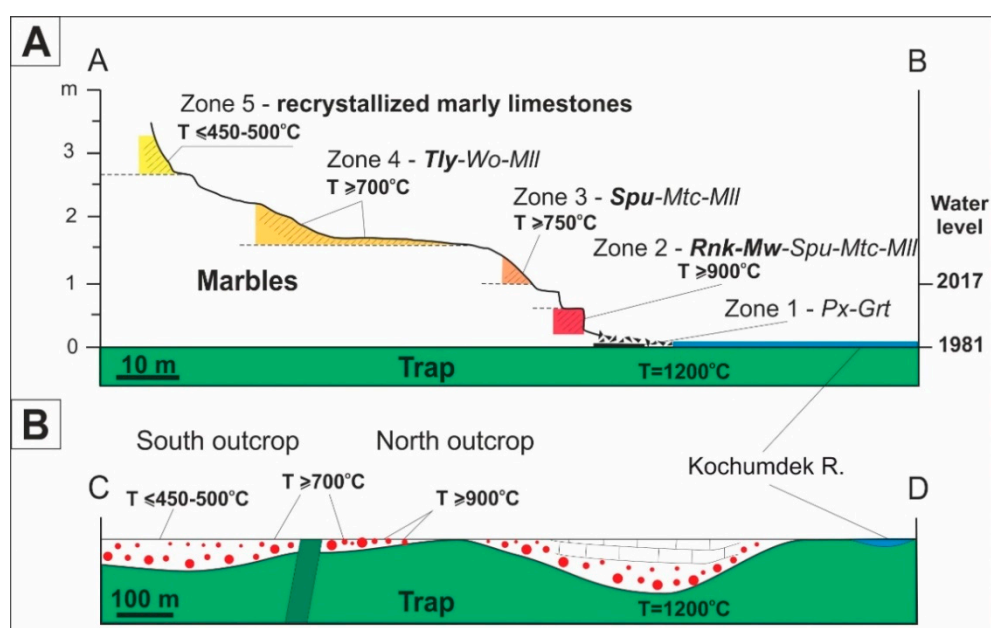


**Figure 4.** Schematic cross sections of sampling site along lines A-B (A) and C-D (B) (symbols are shown in Figure 2). (A) Temperature zoning of the Kochumdek contact aureole. Dash lines correspond to outcropping sampling sites. Left vertical axis shows thickness of metamorphic rocks (m). Zero level is at intrusion top. (B) Simplified profile of the Kochumdek intrusion top. Modified version after [30]. Grt = garnet, Mll = melilite, Mtc = monticellite, Mw = merwinite, Px = pyroxene, Rnk = rankinite, Spu = spurrite, Tly = tilleyite, Wo = wollastonite.

The ~4 m thick (Figure 4A) aureole results from prograde metamorphism of marly limestone by a heat flux rising from the sill, with an initial magma temperature of ~1200 °C. The thermal event produced three high-grade mineral assemblages at progressively closer distances to the contact: (i) calcite + tilleyite + wollastonite + melilite (Zone 4: 1.5–2.6 m), (ii) calcite + spurrite + monticellite + melilite + perovskite (Zone 3: 1.0–1.5 m), and (iii) calcite + spurrite + merwinite + monticellite + melilite + perovskite ( $\pm$  rankinite, bredigite) (Zone 2: 0.3–0.5 m). The edge of the high-grade contact metamorphic aureole at ~2.6 m is marked by an abrupt change from tilleyite-wollastonite marble to recrystallized marly limestone of a similar appearance (Zone 5). The top of the sill is delineated by a very thin (1–3 cm) and discontinuous skarn of Zone 1 [2,30].

The S-T<sub>1</sub> sediments lying over the Kochumdek sill were about 700 m thick at the time of its emplacement in the Early Triassic, which corresponds to a pressure of 200 bar. Based on poly-mineral assemblages in the marbles, the intruding magma is inferred to have heated the sediments to 700 to 900 °C [1,2,30]:  $\geq 900$  °C in Zone 2;  $\geq 750$  °C in Zone 3;

and  $\geq 700$  °C in Zone 4 (Figure 4A); the temperature within Zone 5 recorded in the isobaric invariant assemblage of calcite + actinolite + K-feldspar + diopside + biotite was no higher than 450–500 °C [49]. The P-T conditions of the Kochumdek contact metamorphism have been reliably constrained, which makes it a natural reference system suitable for the study of the ensuing compositional changes.

In general, the aureole is free from evident imprints of closely related metasomatic changes or net transfer reactions. Deformation signatures are rare or absent. The rocks appear virtually homogeneous, free from textural effects of deformation and mechanical mixing (namely, local reorientation or recrystallization of mineral grains, strong preferred orientation, or crystal size patterns). Both sill and metamorphic or sedimentary rocks near the contact lack breccias, cataclastics, healed cracks, or veining networks.

### 3. Material and Methods

#### 3.1. Sampling

About 150 samples of gabbro, marble, and limestone were collected during the field trips of 1981 and 2017 to the Kochumdek River. The highest-grade spurrite-merwinite marbles were sampled in 1981 in the dried riverbed by Dr. V.Yu. Kolobov. The very top of the sill as well as lower-grade marble and marly limestone was sampled in 2017 (Figure 2B–E). The sampling site was a 1-km-long and 70–100-m wide band from the intrusive contact into the sediments (Figure 2A). A total of sixty-six representative samples, including gabbro (12), spurrite (19) and tilleyite (10) marbles, and recrystallized marly limestones (25) were selected for a detailed mineralogical study.

#### 3.2. Analytical Procedures

Analyses were mostly carried out at the Analytical Center for Multi-Elemental and Isotope Research (Sobolev Institute of Geology and Mineralogy (IGM, Novosibirsk, Russia)) and at the South Ural Research Center of Mineralogy and Geoecology (SU FRC MG, Miass, Russia). Major elements in bulk-rock samples were analyzed by the ICP-AES technique (inductively coupled plasma atomic emission spectroscopy) on a ThermoJarrell IRIS Advantage atomic emission spectrometer (ThermoJarrell Intertech Corporation, Atkinson, WI, USA) at IGM (Novosibirsk). The preconditioning procedure included fusion of powdered whole-rock samples with lithium borate [50]. Trace elements in bulk samples of gabbro, marble, and limestone were determined by mass spectrometry with inductively coupled plasma (ICP-MS) on an Agilent 7700x spectrometer (Agilent Technologies, Inc., Santa Clara, CA, USA) at the SU FRC MG (Miass, Russia). The method was slightly modified from those reported in [51,52] and is described in detail by Sokol et al. (2020) [53].

Mineral phases ( $\geq 1\%$ ) were identified by X-ray diffraction analysis (XRD) in powdered samples. All specimens were analyzed on a Shimadzu XRD-600 diffractometer (Shimadzu Corporation, Kyoto, Japan) (CuK $\alpha$  radiation with a graphite monochromator,  $\lambda = 1.54178$  Å). The scans were recorded from 6–60 °2 $\theta$  at 0.05 °2 $\theta$  increments with 5 s scanning time per step.

Scanning electron microscopy (SEM) was used to identify minerals and to characterize the phase distribution and morphology of sulfides, based on energy-dispersive spectra (EDS), backscattered electron (BSE) images, and X-ray element maps (EDS system). The measurements were performed at IGM (Novosibirsk) on a TESCAN MIRA 3LMU microscope (Tescan Orsay Holding, Brno, Czech Republic) equipped with an Oxford AZtec Energy Xmax-50 microanalyses system (Oxford Instruments Nanoanalysis, Abingdon, UK). For SEM examination, thin sections were sputter coated with ~15 to 25-nm carbon films. EDS analyses of minerals were run in a high-vacuum mode at an accelerating voltage of 20 kV, a beam current of 1.5 nA, and a live spectra acquisition time of 20 s. The results were checked against reference standards of simple compounds and metals for most of the elements.

Electron probe microanalyses (EPMA). The mineral chemistry of sulfides was analyzed in  $>10$   $\mu\text{m}$  grains on a JEOL JXA 8100 electron microprobe microanalyzer (JEOL, Tokyo, Japan) in C-coated polished thin sections, at an accelerating voltage of 20 keV, a beam



current of 20 nA, and a peak counting time of 10 s. The compositions of sulfides were determined with reference to standards: synthetic FeS for SK $\alpha$  and FeK $\alpha$ , ZnS for ZnK $\alpha$ , garnet 'IGEM' for MnK $\alpha$ , CuFeS<sub>2</sub> for CuK $\alpha$ , FeNiCo for NiK $\alpha$  and CoK $\alpha$ , albite for NaK $\alpha$ , orthoclase '359-1' for KK $\alpha$ , 'Cl-apatite' for ClK $\alpha$ , RbNbWO<sub>4</sub> for RbL $\alpha$ , CsPrMoO<sub>4</sub> for CsL $\alpha$ , glass Gl-11Ba for BaL $\alpha$ , glass Gl-10 for SrL $\alpha$ , diopside 'B.D.' for CaK $\alpha$ . The detection limits (3 $\sigma$  value) for the elements were 0.02 wt% for K; 0.03 wt% for Na, Ca, Co, and Ni; 0.04 wt% for Cu, Mn, Rb, and Cl; 0.05 wt% for Fe, Zn, S, and Sr; 0.08 wt% for Ba and Cs.

The trace-element composition of sulfides (pyrrhotite, sphalerite and rasvumite) was determined by laser ablation mass spectrometry with inductively coupled plasma (LA-ICP-MS) at the SU FRC MG (Miass, Russia). The LA-ICP-MS analyses were run on a NewWave Research UP-213 laser ablation system coupled with an Agilent 7700x (Agilent Technologies, Inc., Santa Clara, CA, USA) plasma mass spectrometer. The procedure is outlined in [54], with an Nd: YAG UV source, frequency quadruple (wavelength 213 nm) with fluence settings of 2.5–3.5 J/cm<sup>2</sup>, helium cell carrier gas and a gas flow rate of 0.6–0.7 L/min. Polished sections of marble, gabbro, and marly limestone were made using the standard equipment and following the procedure described in [55]. The texture of the samples was examined by SEM with a special focus on inhomogeneities in FeS, ZnS and KFe<sub>2</sub>S<sub>3</sub> crystals (e.g., zoning or mineral inclusions). The large (50–200  $\mu$ m) grains selected for analyses were free from visible inclusions or signatures of alteration. The LA-ICP-MS method was of limited applicability for sphalerite and rasvumite, because they were commonly too small (only 20  $\mu$ m across) and often contained sub-micrometer mineral inclusions. The element contents were calibrated against reference materials of USGS MASS-1 and USGS GSD-1g using <sup>66</sup>Zn as an internal standard for sphalerite, and <sup>57</sup>Fe for pyrrhotite and rasvumite, respectively [56,57]. All mass fractions for USGS MASS-1 and USGS GSD-1g were taken from the GeoReM base preferred values. The calibration standard was analyzed every 10–15 spots to account for the instrument drift. Data processing was carried out using the Iolite software package [58].

Raman spectroscopy was used for express diagnostics of ZnS and MnS polymorphic modifications and to discriminate between djerfisherite and chlorbartonite. Raman spectra were recorded on a Horiba Jobin Yvon LabRAM HR800 spectrometer (Horiba Jobin Yvon S.A.S., Lonjumeau, France). The spectra were excited with a 532-nm green line of a Thorlabs 50-mW power neodymium Nd:YAG laser working at double-harmonic frequency. The radiated laser power was attenuated with optical filters and the beam power onto the sample surface in range 1.5–0.05 mW. The scattered light was recorded by an Andor 1024-channel Peltier-cooled CCD detector (Oxford Instruments, Belfast, Northern Ireland) in a region of 0 to 1000 cm<sup>-1</sup> at a resolution of 2 cm<sup>-1</sup>. The acquisition time for the Raman spectra varied from 10 to 100 min. The excitation was with Olympus objectives at magnification of  $\times 100$  (WD = 0.2 mm) for green line. The Raman spectra were deconvolved into Voigt amplitude functions using the Model S506 Interactive PeakFit software (2002 Spectroscopy Software, Canberra Industries, Meriden, CT, USA) [59]. For method details see [33]. The collected spectra were compared with reference spectra from RRUFF databases (The RRUFF™ Project), as well as with the spectra of synthetic phases.

Sulfur isotopes were measured in hand-picked pyrrhotite monofractions extracted under a binocular microscope from gabbro, marbles, parent and recrystallized marly limestones. Stable isotope analyses was performed at the Central Science Laboratory (CSL) at the University of Tasmania using flash combustion isotope ratio mass spectrometry (varioPYRO cube coupled to Isoprime100 mass spectrometer). Samples between 0.6 and 3.0 mg of mineral is weighed in tin capsules. Evolved sulfur dioxide is trapped and subsequently released into the mass spectrometer after a reference gas measurement. Stable isotope abundances are reported in delta ( $\delta$ ) values, as deviations from conventional standards in parts per mil (‰) from the following equation:

$$\delta X (\text{‰}) = ((R_{\text{sample}}/R_{\text{standard}} - 1) \times 1000) \quad (1)$$

where X = <sup>34</sup>S and R = the ratio <sup>34</sup>S/<sup>32</sup>S.

The  $\delta^{34}\text{S}$  values are reported respective to CDT (Canyon Diablo Troilite). International standards IAEA-S-1, IAEA-S-2, and IAEA-S-3, IAEA-SO5, NBS 123 and NBS 127 were used to correct for instrumental drift and for Quality Assurance purposes. The analytical precision, determined by repetitive measurements of at least three international standards, was around 0.2‰ for  $\delta^{34}\text{S}$  and 0.25‰ for S contents.

## 4. Results

### 4.1. Bulk Rock Chemistry and Mineralogy

#### 4.1.1. Gabbro

The sill at the top of the Kochumdek site consists of fresh, fine-grained (0.5–8 mm) gabbro-dolerite (Figure 3H), which lacks quench zones but contains coarse-grained (up to 2 cm) lenses. The rocks show a large range in major oxides (in wt%): 47.43–50.06 SiO<sub>2</sub>, 1.13–2.03 TiO<sub>2</sub>, 8.33–16.22 Al<sub>2</sub>O<sub>3</sub>, 10.13–13.45 FeO, 5.04–9.97 MgO, 10.20–16.37 CaO, 1.49–3.12 Na<sub>2</sub>O, and 0.39–1.37 K<sub>2</sub>O, and are depleted in MnO (<0.30 wt%) and bulk sulfur (determined as SO<sub>3</sub>) <0.14 wt% (Table 1). Iron (Mg# = 41.71–61.93 mol%) and titanium (1.13–2.03 wt% TiO<sub>2</sub>) enrichment in most of the Kochumdek samples is greater than at the top of the Kuz'movsky sill [42]. The Kochumdek gabbro contain 294–474 ppm V, up to 117 ppm Sc and 241 ppm Cu, moderate amounts of Co (40.7–57.1 ppm) and Ni (40.5–107 ppm), and average Cr, Sr, and Ba contents comparable with those in the Kuz'movsky sill (Table 1; Figure 5A,B).

**Table 1.** Major (in wt%) and trace element compositions (in ppm) of gabbro from the Kochumdek trap and dolerites from the Kuz'movsky sill.

Locality	Kuz'movsky Sill				Kochumdek Trap											
Sample	Mean (n = 8)	S	Min.	Max.	PT-95	PT-95a	PT-96	PT-101	PT-114	PK-4-8	PK-7-1	Mean (n = 7)	S	Min.	Max.	
SiO <sub>2</sub>	49.90	1.00	48.74	51.86	47.43	48.83	48.74	50.06	48.90	48.11	48.35	48.63	0.81	47.43	50.06	
TiO <sub>2</sub>	1.14	0.09	1.00	1.28	2.03	1.81	1.19	1.13	1.60	1.96	1.75	1.64	0.36	1.13	2.03	
Al <sub>2</sub> O <sub>3</sub>	14.99	0.52	14.11	15.81	9.92	10.28	9.43	8.33	15.91	16.22	14.44	12.08	3.33	8.33	16.22	
FeO *	11.22	0.20	10.89	11.47	13.25	12.30	10.13	10.93	12.22	12.64	13.45	12.13	1.21	10.13	13.45	
MnO	0.18	0.01	0.17	0.20	0.27	0.26	0.22	0.22	0.20	0.20	0.23	0.23	0.03	0.20	0.27	
MgO	9.54	1.22	7.86	11.17	6.13	5.86	8.90	9.97	5.04	5.07	6.30	6.75	1.92	5.04	9.97	
CaO	10.11	0.22	9.75	10.40	15.54	15.06	14.83	16.37	11.48	10.26	10.20	13.39	2.65	10.20	16.37	
Na <sub>2</sub> O	2.04	0.15	1.87	2.29	2.00	2.06	2.19	1.49	2.80	3.12	2.72	2.34	0.56	1.49	3.12	
K <sub>2</sub> O	0.75	0.23	0.47	1.18	1.30	1.37	0.87	0.39	0.68	0.84	0.67	0.87	0.35	0.39	1.37	
P <sub>2</sub> O <sub>5</sub>	0.16	0.03	0.11	0.20	0.24	0.26	0.10	0.10	0.19	0.25	0.19	0.19	0.07	0.10	0.26	
SO <sub>3</sub>	na				0.13	0.10	0.14	<0.03	<0.03	0.14	<0.03	0.13	0.02	<0.03	0.14	
LOI	na				0.85	0.91	2.42	0.13	0.10	0.22	0.93	0.79	0.81	0.10	2.42	
Total	100.02				99.09	99.10	99.16	99.15	99.15	99.03	99.26	99.13				
Co	54.1	3.14	50.0	60.0	46.3	45.1	40.7	49.9	43.0	42.2	57.1	46.3	5.62	40.7	57.1	
Ni	184	42.11	129	239	43.8	40.5	86.5	85.9	51.6	76.5	107	70.2	25.23	40.5	107	
Cu	na				136	161	120	88.6	216	241	206	167	55.88	88.5	241	
Zn	na				85.3	79.0	60.4	67.8	102	263	128	112	70.21	60.4	263	
Sc	32.6	2.33	30.0	36.0	79.4	85.2	103	117	44.4	36.2	44.7	72.9	31.69	36.2	117	
V	246	28.75	210	300	415	427	435	474	294	364	336	392	63.10	294	474	
Cr	110	13.43	98.0	135	38.2	36.4	119	128	169	124	138	108	50.61	36.4	169	
Rb	na				17.3	25.6	20.2	8.48	12.7	12.2	10.7	15.3	6.03	8.48	25.6	
Sr	234	20.01	209	271	482	647	513	181	297	290	268	383	166.50	181	647	
Cs	na				0.87	0.61	6.68	0.29	0.21	0.47	1.00	1.45	2.33	0.21	6.68	
Ba	173	15.82	157	201	215	241	147	80.4	150	596	126	222	173.46	80.4	596	
Mg#	60.05	3.03	55.8	63.9	45.22	45.94	61.05	61.93	42.39	41.71	45.51	49.11	8.61	41.71	61.93	

Kuz'movsky sill roof rocks (interval 0–35 m), after [42], \* = all iron is calculated as FeO, LOI = loss on ignition, na = not analyzed, Mg# = 100\*Mg/(Mg + Fe) (mol%), n = number of analyses, Mean = mean value, S = standard deviation, Min = minimum value, Max = maximum value.

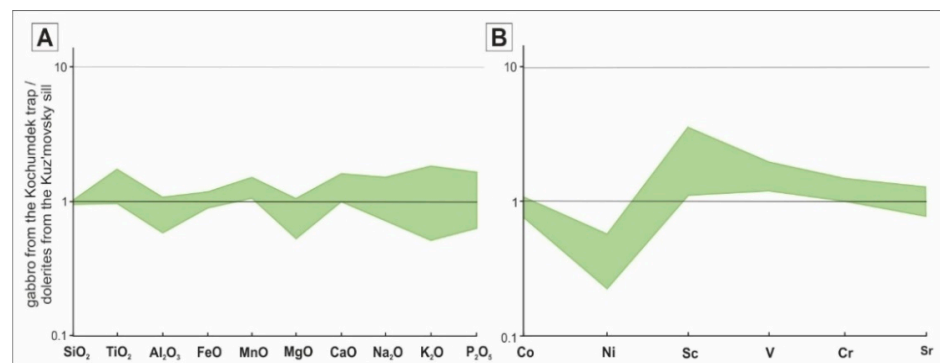


**Figure 5.** Major (A) and trace element (B) patterns for gabbro from the Kochumdek trap, normalized to the Kuz'movsky sill roof rocks (interval 0–35 m), after [42]; based on data from Table 1.

The Kochumdek gabbro consists of ~32–69% plagioclase, ~22–56% clinopyroxene, and  $\leq 6\%$  olivine (Table 2). The majority of plagioclase are fine-grained, interstitial and low-silica varieties, while coarser laths are commonly intergrown with olivine or clinopyroxene (Figure 3I,J). Other phases include minor amounts of coarse flaky biotite (2–10%), as well as brown or greenish-blue acicular amphibole (1–5%) and chlorite (1–4%) that replace pyroxenes. The main accessory minerals are Ti-bearing magnetite, ilmenite, pyrrhotite, chalcopyrite and Cl-bearing fluorapatite. Titanite and pentlandite are sporadic, whereas baddeleyite, zircon, allanite-(Y), zirconolite, sphalerite, cobaltite, troilite and pyrite occur as individual tiny grains (Table 2). Olivine is mostly fayalitic ( $\text{Fa}_{66-69}$ ) with MnO contents no higher than  $\leq 1.0$  wt%. Clinopyroxene commonly occurs as unzoned augite ( $\text{En}_{23-43}\text{Fs}_{15-39}\text{Wo}_{133-45}$ ) or rare pigeonite ( $\text{En}_{25-27}\text{Fs}_{62-67}\text{Wo}_{17-11}$ ) and orthopyroxene ( $\text{En}_{47}\text{Fs}_{49}\text{Wo}_{3}$ ) is extremely rare. Plagioclase laths have distinct zonation with  $\text{An}_{55-82}\text{Ab}_{17-42}\text{Or}_{0.5-2.5}$  cores and  $\text{An}_{51-63}\text{Ab}_{35-46}\text{Or}_{1.6-2.7}$  rims in fine grains and a greater compositional contrast of  $\text{An}_{46-68}\text{Ab}_{30-52}\text{Or}_{1.5-2.7}$  cores and  $\text{An}_{1-19}\text{Ab}_{79-96}\text{Or}_{0.0-2.5}$  rims in coarse laths. Potassium feldspar ( $\text{Or}_{75-100}\text{Ab}_{0-24}\text{An}_{0-3}$ ) occurs as antiperthite in plagioclase or rarely as fine interstitial grains coexisting with Cl-bearing fluorapatite (0.5–2.8 wt% Cl). Biotite (0.1–4.5 wt% Cl), ferro-hornblende (0.4–1.6 wt% Cl), and chlorite (0.1–0.5 wt% Cl) are chlorine-bearing. Biotite contains 29–39 wt% FeO and within 4 wt%  $\text{TiO}_2$  and 1.2 wt%  $\text{V}_2\text{O}_3$ . Magnetite is main carrier of titanium (5.0–16.5 wt%  $\text{TiO}_2$ ) and vanadium (0.5–2.4 wt%  $\text{V}_2\text{O}_3$ ).

**Table 2.** Mineral assemblages of recrystallized marly limestones, marbles and gabbro from the Kochumdek contact aureole (XRD, SEM-EDS, and EPMA data).

Rock Type	Main Phases	Minor Phases	Accessory Phases			
			Oxides, Silicates and Phosphates	Sulfides		
				Matrix	Inclusions	Rims/Cracks
Recrystallized marly limestones <i>n</i> = 25	Calcite	Clinopyroxene (En <sub>28–55</sub> ), Plagioclase (An <sub>72–78</sub> ), K-feldspar (Or <sub>80–98</sub> ), Amphibole, Grossular, Biotite, Chlorite, Quartz	Fluorapatite (F—2.97.4 wt%, Cl—0.1–0.9 wt%), Zircon, Titanite	<b>Pyrrhotite</b> *, <b>Troilite</b> *, Chalcopyrite, <i>Galena</i> , <i>Pyrite</i> , <i>Arsenopyrite</i>	<b>Pyrrhotite</b>	<b>Rasvumite</b> , <b>Djerfisherite</b> , <i>Bartonite</i>
Marbles, Zone 4 <i>n</i> = 10	Calcite, Melilite, Tilleyite, Wollastonite	Kalsilite, Cuspidine	<b>Perovskite</b> Hydroxy-Fluorapatite (F—0.8–5.3 wt%, Cl—0.2 wt%)	<b>Pyrrhotite</b> *, <b>Troilite</b> *, <i>Alabandite</i> , <i>Galena</i> , <i>Acanthite</i>	<b>Pyrrhotite</b>	<b>Rasvumite</b> , <b>Djerfisherite</b> , <i>Bartonite</i>
Marbles, Zone 3 <i>n</i> = 5	Calcite, Melilite, Spurrite, Monticellite	Merwinite, Bredigite	<b>Perovskite</b> , Magnetite	<b>Pyrrhotite</b> *, <b>Troilite</b> *, <i>Alabandite</i> , <i>Sphalerite</i>	<b>Pyrrhotite</b> , <i>Galena</i> , <i>Acanthite</i> , <i>Rasvumite</i> , <i>Alabandite</i> , <i>Sphalerite</i> , <i>Wurtzite</i>	<b>Rasvumite</b> , <b>Djerfisherite</b>
Marbles, Zone 2 <i>n</i> = 14	Calcite, Melilite, Spurrite, Merwinite	Monticellite, Rankinite, Bredigite, Cuspidine	<b>Perovskite</b> , Magnetite, <i>Baghdadite</i> , Hydroxyl-apatite (SiO <sub>2</sub> —5.6–6.1 wt%, SO <sub>3</sub> —2.5–2.6 wt%) <i>Sc-garnet</i> (Sc <sub>2</sub> O <sub>3</sub> —7.7–9.4 wt%)	<b>Pyrrhotite</b> *, <b>Troilite</b> *, <i>Rasvumite</i> , <i>Alabandite</i> , <i>Sphalerite</i>	<b>Pyrrhotite</b> , <i>Galena</i> , <i>Acanthite</i> , <i>Rasvumite</i> , <i>Alabandite</i> , <i>Sphalerite</i> , <i>Wurtzite</i>	<b>Rasvumite</b> , <b>Djerfisherite</b>
Gabbro <i>n</i> = 12	Plagioclase (An <sub>1–82</sub> ), Clinopyroxene (En <sub>23–43</sub> )	Olivine (Fo <sub>31–34</sub> ), Ortoproxene (En <sub>47</sub> ), K-feldspar (Or <sub>75–100</sub> ), Biotite (Cl—0.1–4.5 wt%), Ferro-hornblende (Cl—0.4–1.6 wt%), Chlorite (Cl—0.1–0.5 wt%)	<b>Ti-Magnetite</b> , <b>Ilmenite</b> , <b>Fluor-Chlorapatite</b> (F—1.3–3.8 wt%, Cl—0.5–2.8 wt%), <i>Titanite</i> , <i>Baddeleyite</i> , <i>Zircon</i> , <i>Allanite</i> -(Y), <i>Zirconolite</i>	<b>Pyrrhotite</b> , <b>Chalcopyrite</b> , <i>Troilite</i> , <i>Pentlandite</i> , <i>Sphalerite</i> , <i>Cobaltite</i> , <i>Pyrite</i>		

Main phases (>10 vol%), minor phases (3%–10 vol%) and accessories (<3 vol%): **bold** = dominant phases and *italic* = sporadic phases; *n* = number of samples, \* = in exsolution structures. Contents of F and Cl determined in fluorapatite, chlorapatite; SiO<sub>2</sub> and SO<sub>3</sub> determined in hydroxyl-apatite; Cl determined in biotite, ferro-hornblende and chlorite; and Sc<sub>2</sub>O<sub>3</sub> determined in garnet by SEM-EDS and electron microprobe techniques.

#### 4.1.2. Recrystallized Marly Limestones

Low-grade recrystallized marly limestone has a laminated structure with rhythmically alternating carbonate (up to 1 cm) and silicate (1–3 mm) layers (Figure 3A,B). Correspondingly, major-element concentrations have large ranges (Table 3), except for Na<sub>2</sub>O (<0.5 wt%), K<sub>2</sub>O (<1.60 wt%) and MnO (≤0.14 wt%) (Figure 6A). The sulfur contents reach 0.52–1.61 wt% SO<sub>3</sub>. The average loss on ignition (LOI) is 30.2 wt%, mainly due to CO<sub>2</sub>. With the exception of a few samples with 112–415 ppm Zn, the rocks have low to moderate concentrations of chalcophile elements, though higher than the average in marine Post-Archean limestone [60]: 0.95–27.7 ppm Cu, 5.54–25.9 ppm Ni, and 2.51–12.6 ppm Co (Figure 6B). In particular, there are large ranges spanning up to an order of magnitude for Cr (7.73 to 52.0 ppm), Rb (3.54 to 49.1 ppm), V (5.97 to 69.4 ppm), and Sc (2.26 to 16.1 ppm) (Table 3).

**Table 3.** Major (in wt%) and trace element compositions (in ppm) of recrystallized marly limestones and marbles from the Kochumdek contact aureole (representative samples) compared with Post-Archean limestone.

Rock	Recrystallized Marly Limestones					Marbles					
						Zone 2		Zone 3		Zone 4	
Sample	1	2	3	4	5	6	7	8	9	10	11
	wt%										
SiO <sub>2</sub>	13.66	10.79	14.34	12.92	22.79	10.58	21.04	9.84	13.53	22.75	10.45
TiO <sub>2</sub>	0.10	0.19	0.30	0.26	0.41	0.20	0.45	0.19	0.33	0.40	0.14
Al <sub>2</sub> O <sub>3</sub>	1.76	3.68	4.64	4.08	7.61	3.27	5.79	2.97	4.56	7.19	2.53
Fe <sub>2</sub> O <sub>3</sub> *	0.86	1.54	1.75	1.59	3.14	1.80	3.34	1.83	2.50	2.92	1.31
MnO	0.06	0.07	0.09	0.11	0.14	0.10	0.17	0.12	0.13	0.09	0.05
MgO	10.58	1.37	1.81	1.59	2.54	1.45	2.63	1.43	1.79	2.39	1.38
CaO	34.45	46.94	44.10	45.46	36.99	52.74	51.49	53.60	51.90	44.97	50.76
Na <sub>2</sub> O	0.17	0.17	0.24	0.30	0.42	0.07	0.14	0.08	0.16	0.70	0.12
K <sub>2</sub> O	0.62	0.85	1.07	0.90	1.58	0.04	0.05	0.03	0.12	0.50	0.44
P <sub>2</sub> O <sub>5</sub>	0.05	0.09	0.15	0.10	0.18	0.11	0.14	0.09	0.11	0.17	0.05
SO <sub>3</sub>	na	0.77	0.55	1.26	1.31	1.27	1.65	1.54	1.51	1.57	0.69
LOI	37.30	33.60	30.82	31.47	23.01	27.98	12.85	28.28	23.35	16.00	31.83
Total	99.61	100.06	99.86	100.04	100.12	99.61	99.74	100.00	99.99	99.65	99.75
	ppm										
Co	3.00	4.89	5.91	10.1	12.6	8.03	11.8	6.29	8.21	9.11	2.40
Ni	6.00	11.4	13.4	15.3	23.9	18.1	23.4	17.2	19.1	21.2	6.06
Cu	8.00	6.82	9.14	3.95	27.7	16.7	33.4	11.5	17.3	22.5	7.20
Zn	22.0	415	19.2	19.4	112	38.1	56.2	805	25.0	63.3	7.66
Sc	na	13.0	4.47	3.81	11.6	4.08	9.48	16.1	5.57	10.1	1.85
V	20.0	5.97	21.3	14.8	45.3	6.57	16.8	9.00	15.2	19.6	12.2
Cr	9.00	18.3	16.5	16.6	32.3	19.4	37.7	20.0	23.8	37.9	11.2
Rb	17.0	6.46	17.6	16.4	30.3	1.54	1.77	2.86	4.22	5.67	5.95
Sr	245	427	372	373	306	587	385	412	387	495	226
Cs	na	0.69	0.37	0.77	0.63	<0.01	<0.01	0.05	<0.01	<0.01	0.25
Ba	178	450	61.8	45.1	500	60.2	46.8	61.2	66.3	60.0	249

1 = Mean composition of the Post-Archean limestone, after [60]; \* = all iron is calculated as Fe<sub>2</sub>O<sub>3</sub>, LOI = loss on ignition, na = not analyzed. Samples: 2 = PK-6-1, 3 = PK-4, 4 = PK-5-1, 5 = PK-3-2, 6 = PT-109, 7 = PT-102, 8 = PT-97, 9 = PT-94, 10 = PT-88, 11 = PK-12-1.

The thermal effect caused coarsening of calcite and re-crystallization of fossils in the carbonate layers, whereas the pelitic layers were converted into fine-grained intergrowths dominated by Ca-Mg silicates and feldspars (Table 2; Figure 3A–D). The mineral percentages reach 94–100% calcite, 6% clinopyroxene, and 1% plagioclase in carbonate layers, and 30% calcite, ~40% clinopyroxene (En<sub>28–55</sub>Fs<sub>4–16</sub>Wo<sub>129–68</sub>), 16% low-silica plagioclase (An<sub>72–78</sub>Ab<sub>20–27</sub>Or<sub>1–2</sub>), and 14% K-feldspar (Or<sub>80–98</sub>An<sub>0–14</sub>Ab<sub>2–6</sub>) in metapelites. The contents of other minor phases in the metapelite layers can reach ~8% actinolite, 7% grossular, 5% biotite, 4% chlorite, and <1% quartz; amphibole, micas, and chlorite are Cl-free. Pyrrhotite, a main accessory mineral, is partially replaced by rasvumite and djerfisherite

(or very rarely by bartonite). Chalcopyrite, framboidal pyrite, galena and arsenopyrite are very rare.

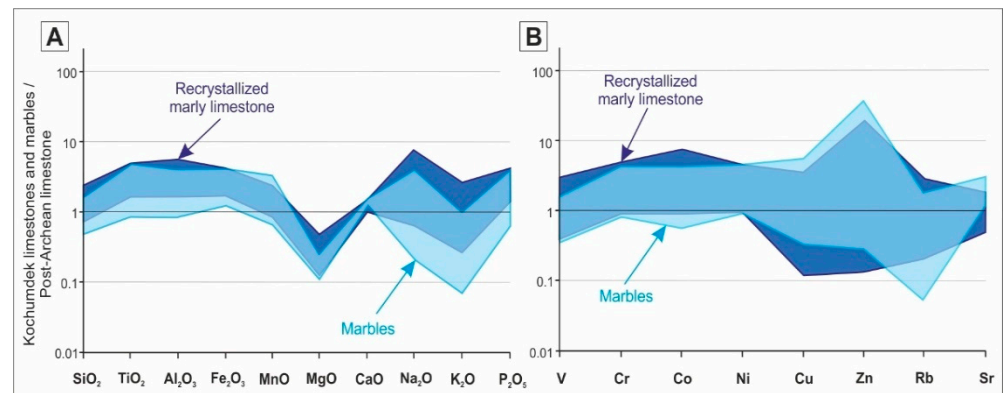


**Figure 6.** Major (A) and trace element (B) patterns for recrystallized marly limestones and marbles from the Kochumdek aureole, normalized to Post-Archean limestone [60]; based on data from Table 3.

#### 4.1.3. Marbles

The Kochumdek marbles are dense fresh rocks with a coarse banded structures consisting of light gray (mainly calcitic) and darker (silicate) bands inherited from the sedimentary protoliths (Figure 3E–G). Merwinite marbles have the coarsest grains of 0.5–4 mm to 1–2 cm [2]. The marbles share major-element similarity with the precursor Lower Kochumdek Subformation marly limestone, except for depletions in  $\text{Na}_2\text{O}$  and  $\text{K}_2\text{O}$  and lower  $\text{CO}_2$  contents (Table 3; Figure 6A). The contents of other major oxides are controlled by silicate-to-carbonate ratios. Spurrinite-merwinite marbles (Zones 2 and 3) show notable variations in  $\text{CaO}$  (50.72–53.67 wt%),  $\text{SiO}_2$  (7.62–21.18 wt%), and  $\text{Al}_2\text{O}_3$  (2.45–5.79 wt%), and have average LOI as high as 24.90 wt% (largely due to  $\text{CO}_2$ ). They have low  $\text{Fe}_2\text{O}_3$  total (1.29–3.45 wt%) and  $\text{MgO}$  (1.17–2.63 wt%), up to 0.20 wt%  $\text{MnO}$ ,  $\text{Na}_2\text{O}$ ,  $\text{K}_2\text{O}$  and  $\text{P}_2\text{O}_5$ , and up to 2.00 wt%  $\text{SO}_3$ . Wollastonite marbles (Zone 4) bear up to 0.70 wt%  $\text{Na}_2\text{O}$ . The Kochumdek marbles are enriched in Zn (up to 805 ppm), contain moderate amounts of Cu (2.92–58.3 ppm), V (5.77–28.7 ppm), Ni (8.27–26.6 ppm), and Cr (10.9–37.8 ppm), and have low contents of Cs (0.05–0.49 ppm), Pb (1.04–7.90 ppm), Co (3.04–12.5 ppm), and Sc (3.21–18.1 ppm). Marbles from all metamorphic zones are depleted in Rb (0.30–7.50 ppm) relative to the average Post-Archean limestone composition (Table 3; Figure 6B).

The Kochumdek marbles consist predominantly of calcite (~51–82%), Ca silicate-carbonates and silicates, including spurrite (~6–49%), tilleyite (~4–11%), and wollastonite (~5–20%), as well as Ca-Mg silicates, such as melilite (~4–47%), merwinite (~1–17%) and monticellite (~3–10%), minor amounts of perovskite ( $\leq 1\%$ ) and sporadic bredigite and rankinite. Calcite contains up to 0.3 wt% of  $\text{MgO}$ ,  $\text{Na}_2\text{O}$  and SrO. Tilleyite ( $\text{Ca}_5\text{Si}_2\text{O}_7(\text{CO}_3)_2$ ), wollastonite ( $\text{Ca}_3\text{Si}_3\text{O}_9$ ), as well as rankinite ( $\text{Ca}_3\text{Si}_2\text{O}_7$ ), have stoichiometric compositions, however, spurrite contains appreciable amounts of P and Na ( $\text{Ca}_{4.9-5.0}\text{Na}_{0-0.1}(\text{Si}_{1.9-2.0}\text{P}_{0-0.1}\text{O}_8)(\text{CO}_3)$ ). Bredigite, merwinite, and monticellite show restricted isomorphic substitution of Mg for Fe and Mn. The ranges of the respective solid solutions are the narrowest for bredigite ( $\text{Ca}_7(\text{Mg}_{0.82-0.85}\text{Fe}_{0.09-0.11}\text{Mn}_{0.02-0.04})(\text{SiO}_4)_4$ ), the largest for monticellite ( $\text{Ca}(\text{Mg}_{0.59-0.82}\text{Fe}_{0.12-0.26}\text{Mn}_{0.03-0.07})(\text{SiO}_4)$ ), and intermediate for merwinite ( $\text{Ca}_3(\text{Mg}_{0.77-0.95}\text{Fe}_{0.05-0.21}\text{Mn}_{0-0.04})(\text{SiO}_4)_2$ ). The compositions of melilite are highly variable and are sensitive temperature indicators [34,61]. Melilite from Zone 4 has high soda-melilite ( $\text{CaNaAlSi}_2\text{O}_7$ , up to 16 mol%) and åkermanite ( $\text{Ca}_2\text{MgSi}_2\text{O}_7$ , up to 68 mol%) contents, whereas that from Zone 2 approaches refractory gehlenite ( $\text{Ca}_2\text{Al}_2\text{SiO}_7$ , up to 80 mol%). The accessories are widespread and randomly distributed, and include perovskite and Fe, K, Zn, Mn, Pb, and Ag sulfides, which mainly occur in the silicate layers (Table 2).

## 4.2. Mineralogical and Textural Relations of Sulfides

### 4.2.1. Gabbro

The gabbro samples from the top of the Kochumdek sill contains minor Fe-Ni-Cu-(Co) sulfide mineralization (Figure 7; Table 2) with pyrrhotite predominantly enclosed in rock-forming minerals and/or in mineral interstices (Figure 8A–C). Pyrrhotite forms coarse  $>150\ \mu\text{m}$  grains or  $150\text{--}400\ \mu\text{m}$  intricate intergrowths, which mostly occur together with chalcocopyrite or less often with Ti-bearing magnetite and ilmenite (Figure 8C–E). In turn, pyrrhotite often encloses thin ( $\leq 5\ \mu\text{m}$ ) lamellae of pentlandite (Figure 9A,B) or more rarely tiny cobaltite and sphalerite inclusions (Figure 8C). Occasionally, sphalerite is localized along the margins of  $100\text{--}150\ \mu\text{m}$  pyrrhotite-chalcocopyrite intergrowths (Figure 9C,D). Troilite occurs as sporadic  $50\text{ to }150\ \mu\text{m}$  inclusions in rock-forming minerals and sometimes hosts  $\leq 25\ \mu\text{m}$  pyrite grains (Figure 8F).

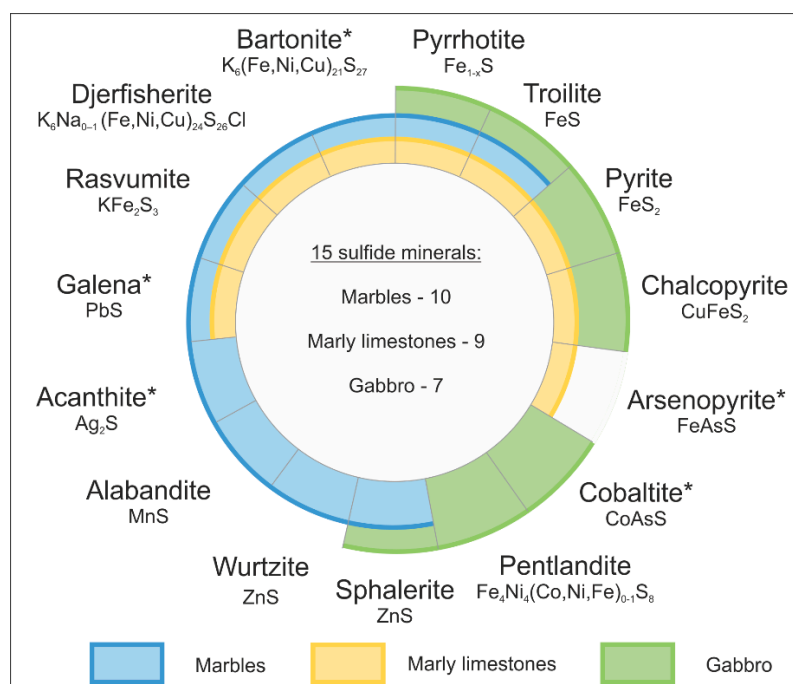


**Figure 7.** Mineralogical diversity of sulfide minerals in marbles, recrystallized marly limestones and gabbro from the Kochumdek contact aureole. \* = small single grains.

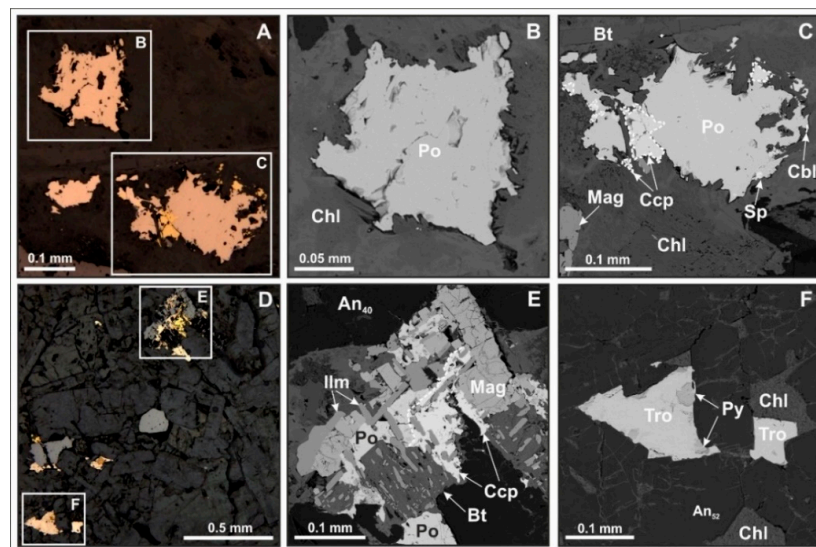


**Figure 8.** Pyrrhotite ( $\text{Fe}_{1-x}\text{S}$ ) and troilite ( $\text{FeS}$ ) from the Kochumdek gabbro. (A,B) Individual pyrrhotite grains. (C) Aggregate of chalcopyrite and pyrrhotite with small cobaltite and sphalerite inclusions. (D,E) Typical intergrowth of accessory phases (Ti-bearing magnetite and ilmenite) with pyrrhotite and chalcopyrite. (D,F) Small troilite grain with pyrite inclusion. (A,D) = optical images in polarized reflected light; (B,C,E,F) = backscattered electron images (BSE). Samples: (A–C) = PK-7-1, (D–F) = PK-4-8. An = anorthite, Bt = biotite, Cbl = cobaltite, Ccp = chalcopyrite, Chl = chlorite, Ilm = ilmenite, Mag = magnetite, Py = pyrite, Po = pyrrhotite, Sp = sphalerite, Tro = troilite.

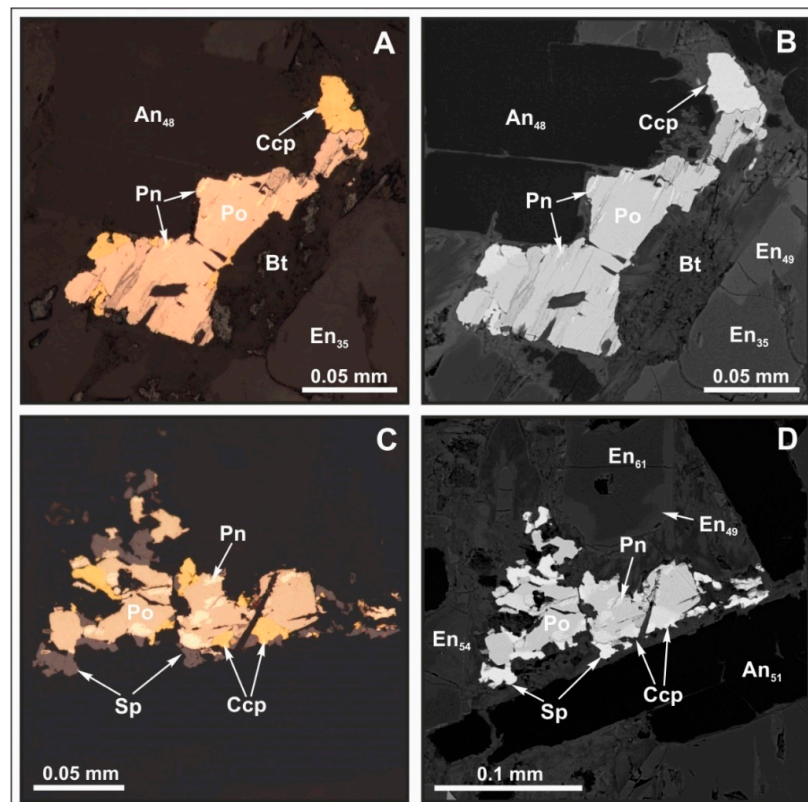
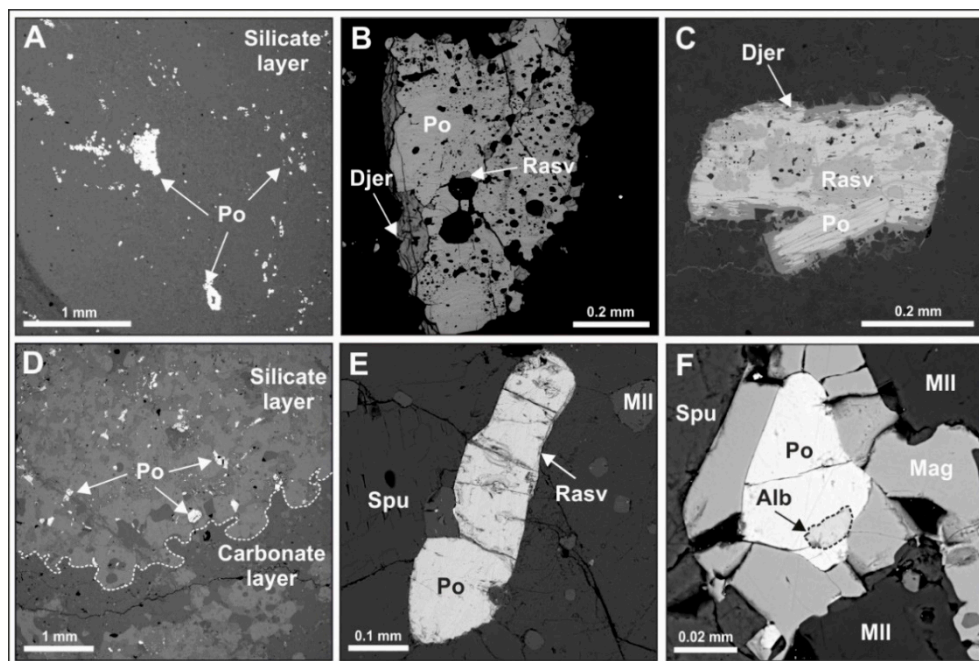


**Figure 9.** Typical intergrowths of multiphase Fe-Cu-Ni-Zn sulfides from the Kochumdek gabbro (sample PK-7-1). (A,C) = optical images in polarized reflected light; (B,D) = backscattered electron images (BSE). An = anorthite, Bt = biotite, Ccp = chalcopyrite, En = enstatite, Pn = pentlandite, Po = pyrrhotite, Sp = sphalerite.



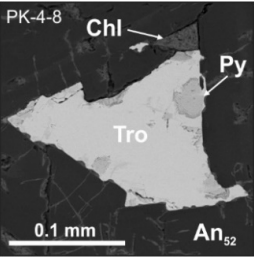
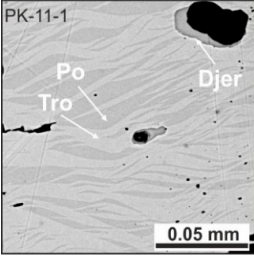
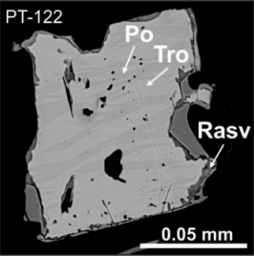
#### 4.2.2. Recrystallized Marly Limestones, Zone 5

The recrystallized marly limestone of Zone 5 (Table 2; Figures 7 and 10A–C) contains abundant sulfide mineralization (six primary and three secondary phases), which is mainly hosted by the metapelitic layers. Pyrrhotite is the most abundant sulfide occurring as 300–700  $\mu\text{m}$  crystals or anhedral grains with a particular spongy structure that records its origin by integrated recrystallization (Figure 10B,C). The mineral encloses thin (1–5  $\mu\text{m}$ ) wavy pyrrhotite-troilite exsolution lamellae, with the Fe/S ratio ranging from 0.9 to 1.0 (Table 4). Framboidal pyrite, which is a common phase in the sedimentary protolith, is very rarely preserved in Zone 5, as well as 3–10  $\mu\text{m}$  inclusions of chalcopyrite, galena and arsenopyrite. Many pyrrhotite grains bear evidence of dissolution and are rimmed by secondary djerfisherite and rasvumite. The rims occasionally contain a phase with a composition resembling Cl-free djerfisherite, which we tentatively interpret as bartonite.



**Figure 10.** Backscattered electron (BSE) image showing the distribution and typical appearance of pyrrhotite grains in recrystallized marly limestones (A–C) and marbles (D–F) from the Kochumdek contact aureole. Recrystallized marly limestones: (A) Distribution and relationship of matrix sulfides (mainly pyrrhotite) hosted by silicate layer. (B,C) Typical anhedral grains of pyrrhotite with a particular spongy structure, partly replaced by later K-Fe sulfides (rasvumite and djerfisherite). Pyrrhotite grains are located in fine-grained silicate layers (calcite + plagioclase + clinopyroxene + K-feldspar). Marbles: (D) Distribution and relationship of sulfide grains (mainly pyrrhotite) in the matrix, located at silicate layers and on boundary with carbonate layers. (E) Typical euhedral pyrrhotite grain with thin rasvumite rim. (F) Pyrrhotite grain is overgrown by magnetite. The boundaries of magnetite rim are roughly parallel and generally mimic the contours of primary pyrrhotite grain with small alabandite inclusion. Samples: A–C = PK-16-1, D–F = PT-104. Alb = alabandite, Djer = djerfisherite, Mag = magnetite, Mll = melilite, Po = pyrrhotite, Rasv = rasvumite, Spu = spurrite.

**Table 4.** Representative analyses and average compositions of pyrrhotite (Fe<sub>1-x</sub>S) and troilite (FeS) from gabbro, recrystallized marly limestones, and marbles from the Kochumdek contact aureole (EPMA data, wt%).

Backscattered Electron Image	Gabbro												
	Mineral	Pyrrhotite ( <i>n</i> = 82)						Troilite ( <i>n</i> = 14)					
Sample	PK-4-8	Mean	S	Min.	Max.	PT-95	Mean	S	Min.	Max.			
	Fe	59.59	61.15	59.79	0.57	58.70	61.15	62.59	61.89	62.95	0.58	61.89	63.82
	Ni	0.43	0.15	0.33	0.23	0.07	0.81	1.17	0.47	0.19	0.34	0.08	1.17
	Co	0.48	0.15	0.23	0.20	0.04	0.66	<0.03	<0.03				
	Cu	0.16	0.05	0.04	0.04	<0.04	0.16	<0.04	<0.04				
	S	40.11	39.10	39.61	0.29	38.75	40.26	36.76	37.47	36.80	0.49	35.99	37.73
	Total	100.96	100.60	99.97				100.52	99.94	99.94			
(Fe + Ni + Co + Cu)/S *	0.87	0.90	0.87				0.99	0.96	0.98				
Recrystallized marly limestones													
Mineral	Pyrrhotite ( <i>n</i> = 11)						Troilite ( <i>n</i> = 8)						
Sample	PK-3-3	PK-4-1	Mean	S	Min.	Max.	PK-3-3	Mean	S	Min.	Max.		
	Fe	61.03	61.53	61.48	0.28	61.03	61.89	62.36	63.80	63.18	0.78	62.24	64.28
	S	38.83	39.07	38.69	0.25	38.33	39.07	37.80	36.24	36.89	0.87	36.05	38.27
	Total	99.86	100.60	100.17				100.16	100.04	100.07			
	Fe/S *	0.90	0.90	0.91				0.95	1.01	0.98			
Marbles													
Mineral	Pyrrhotite ( <i>n</i> = 83)						Troilite ( <i>n</i> = 53)						
Sample	PT-97	PT-122	Mean	S	Min.	Max.	PT-93	PK-16-3	Mean	S	Min.	Max.	
	Fe	61.27	60.87	61.27	0.51	60.07	62.43	63.09	62.91	63.11	0.51	62.06	64.35
	Co	0.12	0.14	0.13	0.01	0.12	0.15	0.09	0.11	0.10	0.01	0.09	0.11
	S	37.95	39.11	38.56	0.49	37.53	39.51	36.80	36.51	36.78	0.38	36.00	37.82
	Total	99.34	100.12	99.96				99.98	99.53	99.99			
(Fe + Co)/S *	0.93	0.89	0.91				0.98	0.99	0.99				

\* =  $\sum \text{Me}/\text{S}$  ratio calculated in atoms per formula unit (a.p.f.u.), formula based on 1 atom of S, Mean = average value, *n* = number of analyses, *S* = standard deviation, Min = minimum value, Max = maximum value. Marbles: PT-93, PT-122 (Zone 2); PT-97 (Zone 3); PK-16-3 (Zone 4). An = anorthite, Chl = chlorite, Djer = djerfisherite, Py = pyrite, Po = pyrrhotite, Rasv = rasvumite, Tro = troilite.

#### 4.2.3. Marbles

##### Sulfides of Merwinite- and Spurrite-Monticellite Zones 2 and 3

The marbles of Zone 2 contain large merwinite grains, along with other ultrahigh-temperature index minerals, including spurrite, gehlenite-rich melilite and sporadic rankinite, and bredigite. Sediments in this zone were heated to temperatures no lower than 900 °C. Some marbles from spurrite-monticellite Zone 3, where the temperature was at least 750 °C, likewise contain merwinite as relict phases or small inclusions.

Sulfide inclusions in the marbles of Zones 2 and 3 are rare and restricted to silicate layers. Almost all such inclusions were found in melilite, except for a few trapped in perovskite, spurrite and monticellite (Table 5; Figure 11). In addition to pyrrhotite (2–30 µm), some melilite grains enclose galena (1–10 µm), acanthite (<1–5 µm), and sporadic Fe-rich sphalerite (up to 10–15 µm). Sulfides usually occur as tiny inclusions in pyrrhotite, commonly in the rim or, very rarely, in the core. Fe-rich MnS (alabandite) similarly occurs as sporadic fine-grained inclusions in pyrrhotite (Figure 10F).

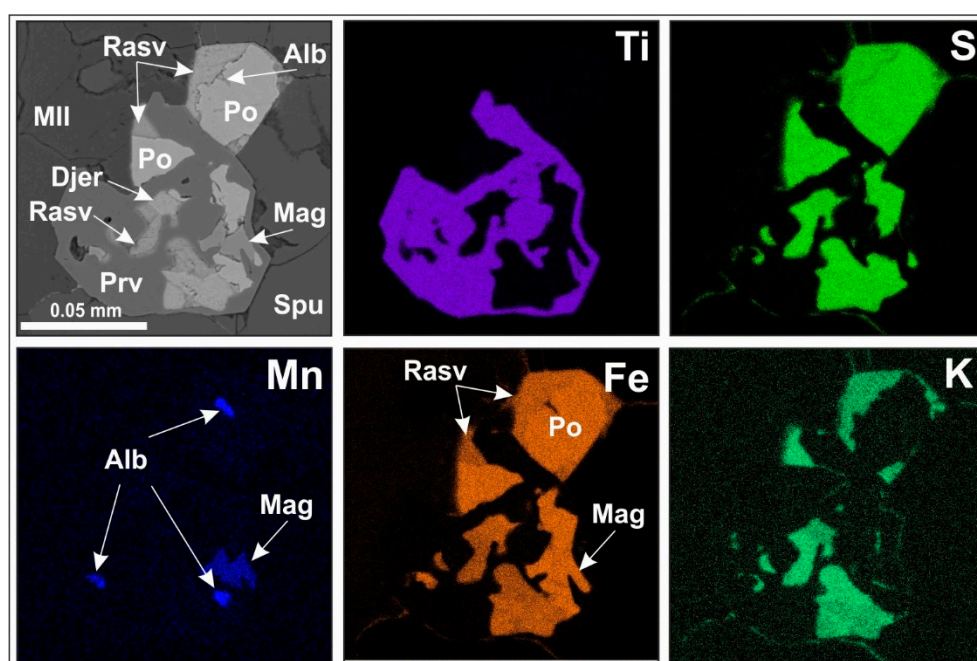


**Figure 11.** BSE image and X-ray elemental maps (Ti, S, Mn, Fe, K) of pyrrhotite pseudo-inclusions partially replaced by rasvumite and djerfisherite. Elemental maps (S, Fe, K) show the presence of tiny fractures, which connect such sulfide grains with the host perovskite. Kochumdek marble, Zone 2, sample PT-99. Alb = alabandite, Djer = djerfisherite, Mag = magnetite, Mll = melilite, Po = pyrrhotite, Prv = perovskite, Rasv = rasvumite, Spu = spurrite.

Pyrrhotite frequently appears as altered pseudo-inclusions, partly or fully replaced by rasvumite, that fits the definition of a retrograde phase according to the criteria of Brown et al. (2014) [27]. The sulfide grains are connected with their melilite or perovskite hosts by tiny cracks resolvable in SEM images (Figure 11). Many pseudo-inclusions contain unaltered blebs of galena, acanthite (<1–5 µm) or (Zn, Fe, Mn) S, like the inclusions of fresh pyrrhotite (Figure 12I).

Table 5. Sulfide minerals found in marbles from the Kochumdek contact aureole.

Mineral	Rock Type Zone	Merwinite Marbles Zone 2			Spurrite-Monticellite Marbles Zone 3			Tilleyite-Wollastonite Marbles Zone 4		
		Matrix	Inclusions	Rims/Cracks	Matrix	Inclusions	Rims/Cracks	Matrix	Inclusions	Rims/Cracks
Pyrrhotite *	Fe <sub>1-x</sub> S	▲	▲		▲	▲		▲	▲	
Troilite *	FeS	▲			▲			▲		
Alabandite	(Mn,Fe)S	●	□		●	□		●		
Sphalerite	(Zn,Fe,Mn)S	●	□		●	□				
Wurtzite	(Zn,Mn,Fe)S		□			□				
Galena	PbS		●			●		□		
Acanthite	Ag <sub>2</sub> S		●			●		□		
Rasvumite	KFe <sub>2</sub> S <sub>3</sub>	●	□	▲		□	▲			▲
Djerfisherite	K <sub>6</sub> (Fe,Ni,Co,Cu) <sub>25</sub> S <sub>26</sub> Cl			●			●			●
Bartonite	K <sub>6</sub> Fe <sub>21</sub> S <sub>27</sub>									□

▲ = main phase, ● = subordinate phase, □ = minor phase, \* = in exsolution structures.

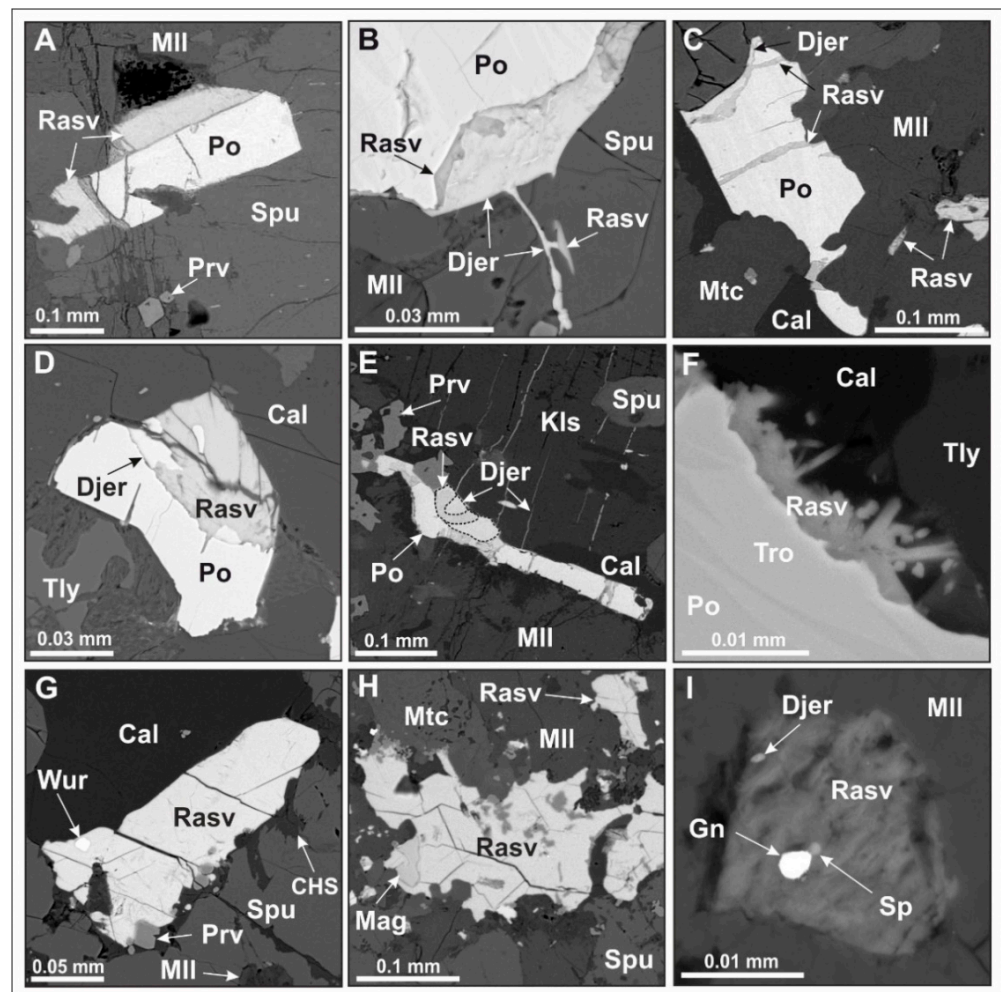


**Figure 12.** Rasvumite and djerfisherite from the Kochumdek marbles (backscattered electron (BSE) images). (A) Pyrrhotite grain overgrown by rasvumite. This kind of pyrrhotite-rasvumite boundary is usually even in shape and free from dissolution features. (B–E) Typical double-layered rims, where rasvumite and djerfisherite compose the inner (adjacent to pyrrhotite) and outer boundaries, correspondingly. Crack-filling djerfisherite in pyrrhotite (C), spurrite (B) and kalsilite (E). (F) Rasvumite microcrystals in the crack at the contact between replacement rim around pyrrhotite, calcite and tilleyite. (G,H) Large rasvumite grains with perfect cleavage ( $60$  or  $120^\circ$  angles between cleavage directions) and inclusions of wurtzite, perovskite and magnetite. (I) Pyrrhotite pseudo-inclusion in melilite completely replaced by aggregates of needle-like rasvumite-II; blebs of galena and sphalerite are preserved as micro-inclusion in rasvumite matrix. Marbles: A, G, H, I (Zone 2), B, C (Zone 3), D–F (Zone 4). Samples: A, I = PT-102, B = PT-97, C = PT-94, D = PT-88, E = PT-89, F = PK-16-3, G = PT-107, H = PT-93. Cal = calcite, CHS = Ca-hydro-silicates, Djer = djerfisherite, Gn = galena, Kls = kalsilite, Mag = magnetite, Mll = melilite, Mtc = monticellite, Mw = merwinite, Po = pyrrhotite, Prv = perovskite, Rasv = rasvumite, Rnk = rankinite, Sp = sphalerite, Spu = spurrite, Tly = tilleyite, Tro = troilite, Wur = wurtzite.

Thus, sulfide inclusions in the marbles of high-temperature Zones 2 and 3 are commonly of Fe, Pb, and Ag compositions (pyrrhotite, galena, and acanthite), while Mn and Zn sulfides are limited to a few cases in pyrrhotite, and phases of Cu, Co, and Ni are absent.

Sulfide grains in the matrix are relatively abundant (up to 1%), diverse (Table 5), and localized in silicate layers or at their boundary with the carbonate layers. No sulfides were found in the matrix of calcite layers. Sulfide inclusions in calcite (mainly pyrrhotite and very rare unidentified varieties of ZnS) are extremely rare and restricted to the carbonate-silicate boundary.

Matrix sulfides are generally much larger than sulfide inclusions and reach up to 500  $\mu\text{m}$  in size (Figure 10D). These include Fe, Zn, K, and Mn compounds (Table 5), which are dominated by subhedral or euhedral pyrrhotite (100–500  $\mu\text{m}$ ) at the boundaries of spurrite, melilite and calcite grains (Figure 10E). Pyrrhotite shows typical exsolution textures with fine ( $\leq 10$   $\mu\text{m}$ ) lamellae and Fe/S ratio ranging from 0.9 to 1.0 (Table 4). Some pyrrhotite grains in samples from Zones 2 and 3 are overgrown by Mn-bearing magnetite containing 0.6 wt%  $\text{TiO}_2$  and up to 150 ppm  $\text{V}_2\text{O}_5$ . The inner and outer boundaries of  $\leq 30$   $\mu\text{m}$  magnetite rims are roughly parallel and generally mimic the contours of the primary pyrrhotite grains (Figure 10F), which indicates overgrowth without replacement reactions. Some matrix pyrrhotite grains host 10–30  $\mu\text{m}$  inclusions of alabandite, sphalerite or wurtzite (Figure 10F) and tiny blebs of galena and acanthite. The textural control of their distribution is independent of lamellae edges.

Alabandite commonly occurs as euhedral inclusions (10–15  $\mu\text{m}$ ) near the edges of large pyrrhotite grains (Figure 10F) or more rarely forms platy inclusions (2–15  $\mu\text{m}$  in width and 300–400  $\mu\text{m}$  in length) or 50–100  $\mu\text{m}$  round grains intergrown with pyrrhotite.

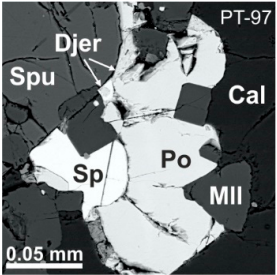
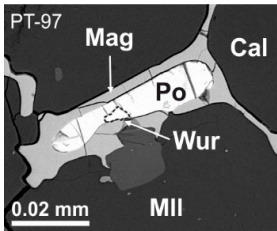
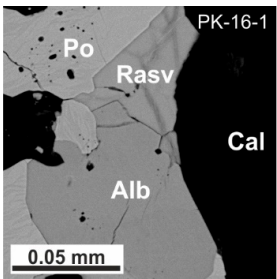
Sphalerite occurs exclusively in the highest-grade marbles as 80–100  $\mu\text{m}$  anhedral grains commonly intergrown with pyrrhotite (Table 6). Wurtzite, identified by Raman spectroscopy, forms sporadic 3–20  $\mu\text{m}$  inclusions in matrix pyrrhotite or less often in coarse rasvumite-I grains (Table 6; Figure 12G).

The (Mn,Fe)S and (Zn,Fe,Mn)S modifications were identified by Raman spectroscopy. Wide absorption bands at  $\sim 228$  and  $\sim 342$   $\text{cm}^{-1}$  in the Raman spectra of the (Mn,Fe)S phase represent an  $\alpha$ -MnS modification ( $Fm\bar{3}m$ ) [62] corresponding to alabandite. Wurtzite is identifiable from the 348, 419, and 628  $\text{cm}^{-1}$  bands that fit the 350,  $\sim 418_{\text{mon}}$ , and  $\sim 630$   $\text{cm}^{-1}$  bands of standard  $\text{ZnS}_{\text{hex}}$  [63]. The Raman spectra of Fe-bearing sphalerite show two strong bands at 301 and 330  $\text{cm}^{-1}$  and match with the 300 and 331  $\text{cm}^{-1}$  bands in the synthetic compound  $(\text{Zn}_{0.84}\text{Fe}_{0.16}\text{S})_{\text{cub}}$  [64].

Up to 400  $\mu\text{m}$  single-phase rasvumite grains with perfect cleavage (i.e., 60 or 120° angles between cleavage directions) frequently grow interstitially in merwinite marbles (Figure 12G,H). They host 10–20  $\mu\text{m}$  inclusions of Zn-Mn-Fe sulfides (mainly wurtzite), magnetite, perovskite, and rarer submicron blebs of galena. This rasvumite is neither intergrown with pyrrhotite nor replaced by later djerfisherite. We interpret this rasvumite as an early generation (rasvumite-I) prograde phase, unlike widespread aggregates of fine-grained secondary rasvumite-II, which replaces pyrrhotite during retrogression and commonly coexists with djerfisherite.

Thus, the marbles from high-temperature Zones 2 and 3 share similarities between the inclusion and matrix assemblages. They mainly consist of Fe, Mn, Zn, Pb, and Ag sulfides (e.g., pyrrhotite, Zn-Mn-Fe sulfides, galena, and acanthite). Single-crystal rasvumite-I occurs only in the matrix, whereas rasvumite in inclusions are rather a retrograde secondary phase that replaces pyrrhotite. Cu, Co and Ni phases are absent and the presence of these elements was not detected in SEM-EDS point analyses of pyrrhotite or rasvumite-I in both inclusion and matrix assemblages from the highest-grade metamorphic zones.

Table 6. Representative analyses and average compositions of Zn-Fe-Mn and Mn-Fe sulfides from the Kochumdek marbles (SEM-EDS data).

Mineral/Backscattered Electron Image	Element	Fe	Mn	Zn	Cd	S	Total	Fe	Mn	Zn	Cd	$\Sigma$ Me	
	Sample	wt%						a.p.f.u.					
	PT-97	17.92	7.43	38.91	0.50	34.44	99.20	0.299	0.126	0.554	0.004	0.983	
	PT-97	18.26	4.50	41.68	0.54	34.17	99.15	0.307	0.077	0.598	0.005	0.986	
	PT-97	21.87	5.26	37.18	0.47	34.34	99.12	0.366	0.089	0.531	0.004	0.990	
	PT-97	19.07	5.87	39.40	0.64	34.52	99.50	0.317	0.099	0.560	0.005	0.981	
	PT-97	20.65	4.01	40.03	0.38	34.27	99.34	0.346	0.068	0.573	0.003	0.990	
	PT-97	19.82	5.06	39.47	0.44	34.46	99.25	0.330	0.086	0.562	0.004	0.981	
	PT-97	1.11	0.90	1.12	0.08	0.38							
	PT-104	8.86	16.30	39.35	<0.30	35.32	99.83	0.144	0.279	0.566	0.000	0.989	
	PT-93	10.52	17.74	36.68	<0.30	34.69	99.13	0.174	0.290	0.519	0.000	0.983	
	PT-97	19.06	16.84	28.48	<0.30	35.48	99.86	0.308	0.277	0.394	0.000	0.979	
	PT-97	12.03	18.25	33.33	<0.30	35.54	99.15	0.194	0.300	0.500	0.000	0.994	
	PT-97	12.37	16.96	34.66	<0.30	35.07	99.06	0.202	0.282	0.500	0.000	0.984	
	PT-97	4.78	0.94	4.69		0.51							
	PT-97	7.86	16.00	28.48		34.57							
	PT-102	10.54	52.95	<0.30	<0.30	35.80	99.29	0.169	0.863	0.000	0.000	1.032	
	PT-97	7.49	56.22	<0.30	<0.30	36.78	100.49	0.117	0.892	0.000	0.000	1.009	
	PT-88	12.19	50.45	<0.30	<0.30	36.97	99.61	0.189	0.796	0.000	0.000	0.986	
	PK-16-1	15.68	47.18	<0.30	<0.30	36.31	99.17	0.248	0.758	0.000	0.000	1.006	
	PK-16-1	10.24	53.03	<0.30	<0.30	36.60	99.87	0.161	0.849	0.000	0.000	1.010	
	PK-16-1	2.28	2.51			0.28							
	PK-16-1	7.49	47.18			35.80							
PK-16-1	15.68	56.22			36.97								

a.p.f.u. = atoms per formula unit, formula based on 1 atom of S, Mean = average value,  $n$  = number of analyses,  $S$  = standard deviation, Min = minimum value, Max = maximum value,  $\Sigma$  Me = Fe + Mn + Zn. Marbles: PT-93, PT-102, PT-104 (Zone 2); PT-97 (Zone 3); PT-88, PK-16-1 (Zone 4). Alb = alabandite, Cal = calcite, Djer = djerfisherite, Mag = magnetite, Mll = melilite, Po = pyrrhotite, Rasv = rasvumite, Sp = sphalerite, Spu = spurrite, Wur = wurtzite.

#### Sulfides of Tilleyite-Wollastonite Zone 4

The pelitic layers of marly limestone in Zone 4 are decarbonated over ~1.5 m from the contact, with formation of lower-temperature ( $T \geq 700$  °C) assemblages of wollastonite + Na-enriched melilite + tilleyite + perovskite.

Sulfide inclusions in this zone are mainly <10 µm pyrrhotite grains usually trapped in melilite rims. Tiny blebs of alabandite, galena, and acanthite are very rare and are commonly enclosed in pyrrhotite (Table 5). Pyrrhotite is the only matrix sulfide and occurs as grains up to 500 µm in size with thin lamellae of troilite. In addition, pyrrhotite is occasionally intergrown with up to 100 µm round grains of alabandite (Table 6), but more often contains the latter as fine inclusions.

#### Retrograde Sulfides

Retrograde sulfides in the Kochumdek marbles include K-Fe minerals, such as abundant rasvumite-II with minor bartonite and K-Fe( $\pm$  Cu, Ni) sulfide-chloride (djerfisherite) (Table 5; Figures 12 and 13). Djerfisherite and rasvumite-II (unlike prograde rasvumite-I) are common in all metamorphic zones but are absent in the sill top. Rasvumite-II commonly occurs in pyrrhotite reaction rims where the two phases are separated by a dissolution boundary which has an uneven profile. Pyrrhotite is partly replaced, and rasvumite-II crystallizes asymmetrically, being thickest on the crack-facing side of pyrrhotite grains. The rasvumite rims are the thinnest next to the contact melilite and monticellite (up to 15 µm) but reach 50–70 µm at the boundary with spurrite (Figure 12B,C). Many rims of this kind are double-layered, with a wider rasvumite-II zone adjacent to pyrrhotite and a thin and discontinuous outer zone of djerfisherite (Figure 12B–E). Rasvumite-II microcrysts are limited to a few cases where rims have expanded into the open crack space (Figure 12F). Fully replaced pyrrhotite grains were not observed in the matrix but often appear as pseudo-inclusions (Figure 12I), while the tiny blebs of galena, (Zn, Fe, Mn) polymorphic modifications, alabandite, and acanthite remain intact (Figure 13). Less often, rasvumite overgrows around pyrrhotite rather than replacing it, where it forms rims up to 85 µm thick. This kind of pyrrhotite-rasvumite boundary is usually even in shape and free from dissolution features (Figure 12A).

Djerfisherite commonly follows and replaces rasvumite-II, or more rarely fills thin cracks in pyrrhotite and in some adjacent silicates (spurrite, melilite, kalsilite) (Figure 12B–E). Its identification is based on optical microscopy, SEM-EDS, and Raman spectroscopy data. The most intense Raman bands of the Kochumdek djerfisherite (98, 118–135, 178, 269, 321  $\text{cm}^{-1}$ ) are almost identical to those of a synthetic  $\text{K}_6\text{Fe}_{24}\text{S}_{26}\text{Cl}$  (cub) compound: 95, 121–137, 179, 270, and 323  $\text{cm}^{-1}$  [33].

Bartonite is a tetragonal analog of cubic djerfisherite with variable contents of Cl and S, where Cl may be absent in the ultimate (end-member) case [65–67]. The Cl-free analogs of djerfisherite in the Kochumdek aureole coexist with secondary rasvumite and djerfisherite phases in Zones 4 and 5. The identification of bartonite is quite tentative and stems from the absence of Cl in the SEM-EDS spectra. XRD and Raman analyses were hampered due to the small grain sizes and intricate intergrowths of bartonite with other K-Fe sulfides. Retrograde sulfide mineralization is especially abundant in the marbles of Zone 4, where pyrrhotite is most strongly affected by dissolution and partially-to-completely replaced by retrograde rasvumite-II, djerfisherite and bartonite (Figure 13).



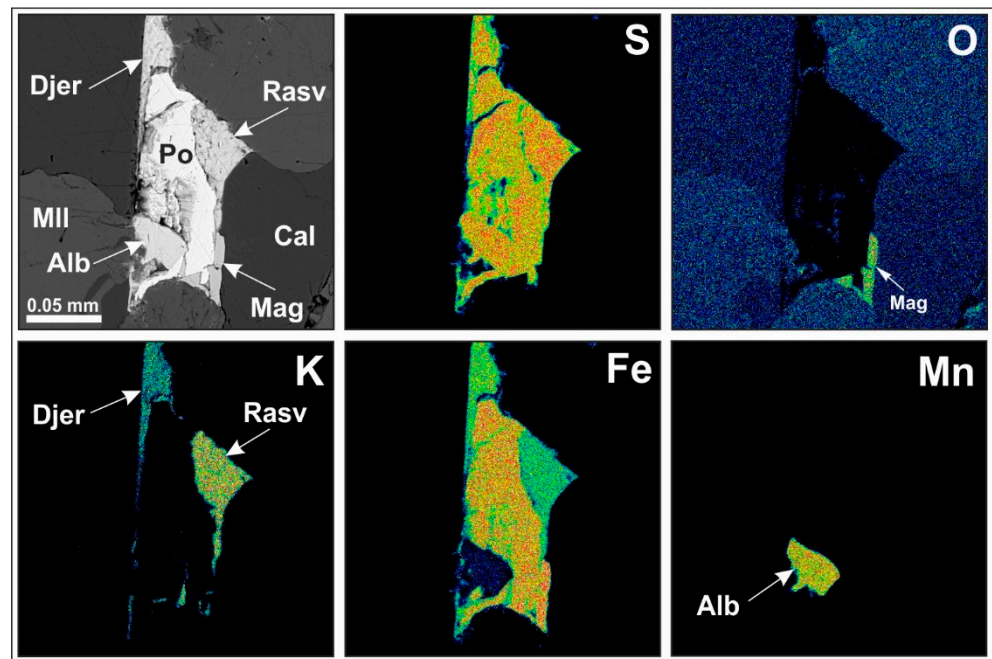


**Figure 13.** BSE image and X-ray elemental maps (S, O, K, Fe, Mn) showing partly replacement of pyrrhotite by later K-sulfides (rasvumite and djerfisherite) and remained intact alabandite inclusion (Kochumdek marble, Zone 4, sample PT-88). Alb = alabandite, Cal = calcite, Djer = djerfisherite, Mag = magnetite, Mll = melilite, Po = pyrrhotite, Rasv = rasvumite.

#### 4.3. Mineral Chemistry of Sulfides

##### 4.3.1. Gabbro

Most of the sulfides in the gabbro samples from the top of the Kochumdek sill are solid solutions, except for chalcopyrite and pyrite, which correspond to the ideal compositions. Pentlandite ( $\text{Fe}_{3.71-4.92}\text{Ni}_{2.79-4.33}\text{Co}_{0.49-1.71}\text{S}_8$ ) shows large ranges of Fe (27.10 to 37.32 wt%), Ni (21.92 to 32.84 wt%) and Co (3.78 to 13.16 wt%). Sphalerite contains 10.63–12.40 wt% Fe ( $\text{Zn}_{0.68-0.78}\text{Fe}_{0.18-0.32}\text{S}$ ). Troilite with  $(\text{Fe} + \text{Ni})/\text{S} = 0.96-0.99$  bears up to 1.17 wt% Ni. SEM-EDS and EPMA of gabbro-hosted pyrrhotite reveal systematic presence of Ni, Co, and Cu reaching, respectively, 0.81 wt%, 0.66 wt%, and 0.16 wt% (Tables 4 and 7). LA-ICP-MS analysis of coarse pyrrhotite grains confirms the concentration of Co (3643–5260 ppm) and Ni (3027–9230 ppm) and reveals additional impurities of  $\leq 192$  ppm Se and  $< 65$  ppm Mn (Table 8; Figure 14). Other chalcophile elements are minor: 1.49 to 6.83 ppm Ag, V, As, Pb, Hg, Ge, Mo, Zn, and Cu, and 0.20 to 0.69 ppm Os, Ru, Tl, Pd, Bi, Te, Ga, and Sn. The trace-element compositions of cobaltite (CoAsS), sphalerite, and pentlandite remain unconstrained because of small grain sizes.

**Table 7.** Average compositions of sphalerite, chalcopyrite, pyrite, and pentlandite from gabbro of the Kochumdek trap roof (EPMA data, wt%).

Mineral		Element						Total
		Fe	Ni	Co	Cu	Zn	S	
Sphalerite <i>n</i> = 10	Mean	11.76	0.13	0.23	0.49	53.15	34.02	99.78
	S	0.54	0.20	0.06	0.37	0.66	0.13	
	Min	10.63	0.05	0.16	0.15	52.23	33.87	
	Max	12.40	0.57	0.33	1.18	54.40	34.25	
Chalcopyrite <i>n</i> = 35	Mean	30.79	<0.03	<0.04	34.01	0.06	34.97	99.83
	S	0.29			0.26	0.09	0.21	
	Min	30.24			33.38	<0.05	34.50	
	Max	31.42			34.43	0.41	35.43	
Pyrite <i>n</i> = 10	Mean	46.13	0.34	0.13	<0.04	<0.05	52.88	99.49
	S	0.67	0.42	0.03			0.35	
	Min	45.01	0.05	0.07			52.55	
	Max	46.78	1.14	0.20			53.53	
Pentlandite <i>n</i> = 12	Mean	31.54	28.58	5.60	<0.04	<0.05	33.85	99.57
	S	3.25	3.64	2.51			0.52	
	Min.	27.10	21.92	3.78			33.14	
	Max.	37.32	32.84	13.16			35.01	

Mean = average value, *n* = number of analyses, *S* = standard deviation, Min. = minimum value, Max. = maximum value.

**Table 8.** Average trace element compositions of pyrrhotite from recrystallized marly limestones, marbles, and gabbro from the Kochumdek contact aureole (LA-ICP-MS data, ppm).

Rock Type	Element	Mn	Co	Ni	Cu	Zn	Se	Mo	Ag
Recrystallized marly limestones <i>n</i> = 17	Mean	151	485	655	1.72	1.56	6.81	0.49	0.12
	S	65.6	14.5	159	1.00	0.63	5.47	0.18	0.18
	Min	61.0	465	343	1.02	0.99	2.10	0.23	<0.01
	Max	263	517	808	4.10	3.09	23.1	0.97	0.75
Tly-Wo marbles, Zone 4 <i>n</i> = 10	Mean	342	345	909	50.9	9.60	3.35	0.02	0.14
	S	235	101	523	41.9	11.1	1.61	0.02	0.14
	Min	72.4	186	180	2.35	1.38	3.10	0.01	0.02
	Max	733	569	1751	116	34.6	4.40	0.05	0.39
Spu-Mtc marbles, Zone 3 <i>n</i> = 18	Mean	258	410	242	15.3	17.2	4.96	<0.01	0.08
	S	99.4	72.6	276	10.9	12.5	2.63		0.07
	Min	135	278	16.7	1.67	0.98	3.70		<0.01
	Max	509	515	913	32.1	35.9	6.50		0.22
Spu-Mw marbles, Zone 2 <i>n</i> = 4	Mean	182	349	7.63	<0.02	1.02	6.00	<0.01	0.04
	S	67.2	61.4	2.68		0.54	2.86		
	Min	112	297	4.57		0.83	3.20		0.04
	Max	246	417	9.56		1.22	9.90		0.04
Gabbro <i>n</i> = 16	Mean	15.8	4422	6051	41.7	6.44	136	6.39	1.71
	S	15.2	447	1850	49.6	5.15	16.4	5.20	1.93
	Min	3.20	3643	3027	1.67	2.19	121	1.57	0.21
	Max	64.9	5260	9230	159	17.9	192	20.7	6.40

Mean = average value, *n* = number of analyses, *S* = standard deviation, Min = minimum value, Max = maximum value. Pyrrhotite from recrystallized marly limestone contains 0.72 ppm Hg, 0.29 ppm Tl; from Tly-Wo marbles (Zone 4) contains 0.13 ppm In, 0.11 ppm Cd and Tl; from Spu-Mtc marbles (Zone 3) contains 1.41 ppm Cd; and from gabbro contains 6.23 ppm Hg, 0.62 ppm Tl. Mtc = monticellite, Mw = merwinite, Spu = spurrite, Tly = tilleyite, Wo = wollastonite.

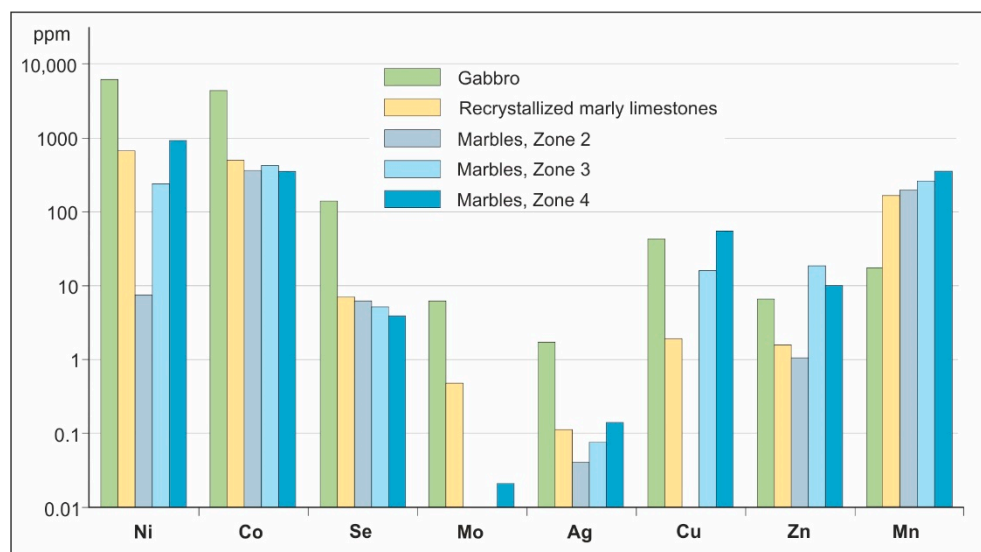


**Figure 14.** Average trace element compositions of pyrrhotite from gabbro, recrystallized marly limestones, and marbles from the Kochumdek contact aureole; based on LA-ICP-MS data (Table 8).

#### 4.3.2. Recrystallized Marly Limestones

Impurities in pyrrhotite from the limestone samples are especially diverse, though the contents of trace elements are low. Coarse pyrrhotite grains are homogeneous, with minor Mn, Co, and Ni impurities (151–655 ppm in average) and orders of magnitude lower contents of Ge, V, Mo, Pb, Zn, Cu, and Se (1.27–7.03 ppm). Other minor impurities include Ag, Sn, Sb, Ga, and Bi (0.12–0.75 ppm) and, locally, up to 0.18 ppm Tl, 0.72 ppm Hg, and 0.94 ppm Te (Table 8; Figure 14). Chalcopyrite, pyrite, and rasvumite ( $K_{0.95-0.97}Fe_{1.93-1.97}S_3$ ) approach the ideal compositions. Retrograde K-Fe sulfides are devoid of Co and bear the lowest Ni and Cu concentrations: djerfisherite ( $K_{6.04-6.11}Fe_{23.05-23.73}Ni_{0.0-0.83}S_{26}Cl_{0.74-0.90}$ ) contains  $\leq 2.00$  wt% Ni, while bartonite ( $K_{5.96-6.03}Fe_{20.35-20.92}Cu_{0.17-0.25}Ni_{0.0-0.19}S_{27}$ ) includes  $< 0.50$  wt% Ni and  $\leq 0.71$  wt% Cu.

#### 4.3.3. Marbles

Pyrrhotite ( $Fe_{1-x}S$ ) from the highest-temperature merwinite assemblages of Zone 2 ( $T \geq 900$  °C) has a pure composition, with low contents of all trace elements, except for Co ( $\leq 0.15$  wt%) and within 246 ppm Mn, 10 ppm Ni and Se, and 1 ppm Zn. Pyrrhotite from spurrite-monticellite assemblages in Zone 3 ( $T \geq 750$  °C) has comparable contents of Co, Se, and Ag reaching 515 ppm, 3.70 to 6.50 ppm, and 0.22 ppm, respectively, but contains more Ni and Mn (up to 913 ppm and 509 ppm, respectively). The contents of Zn ( $\leq 36$  ppm) and Cu ( $\leq 32$  ppm) are about ten times higher than the respective values for Zone 2 (Tables 4 and 8; Figure 14).

Pyrrhotite from the lower-temperature tilleyite-wollastonite assemblages of Zone 4 ( $T \geq 700$  °C) occasionally shows enrichments reaching 1751 ppm Ni, 733 ppm Mn, and 569 ppm Co, but has low Cu (within 116 ppm), Zn (35 ppm), and Se (4.40 ppm), and negligible contents of Ag ( $\leq 0.40$  ppm) and Mo ( $< 0.05$  ppm) (Table 8; Figure 14).

Alabandite grains are homogeneous and have a large range of MnS/FeS ratios ( $Mn_{0.76-0.89}Fe_{0.12-0.25}S$ ) (Figure 15). The range of (Mn,Fe)S solid solutions narrows down with increasing temperature of metamorphism. The contents of Fe are especially variable (7.53 to 15.68 wt%) in alabandite from Zone 4, but is from 8.24 to 11.53 wt% in Zone 2 and 7.49 to 9.99 wt% in Zone 3 (Table 6). The mineral is free from Mg, Cr, and V impurities, which are common in high-temperature alabandite from meteorites [68].

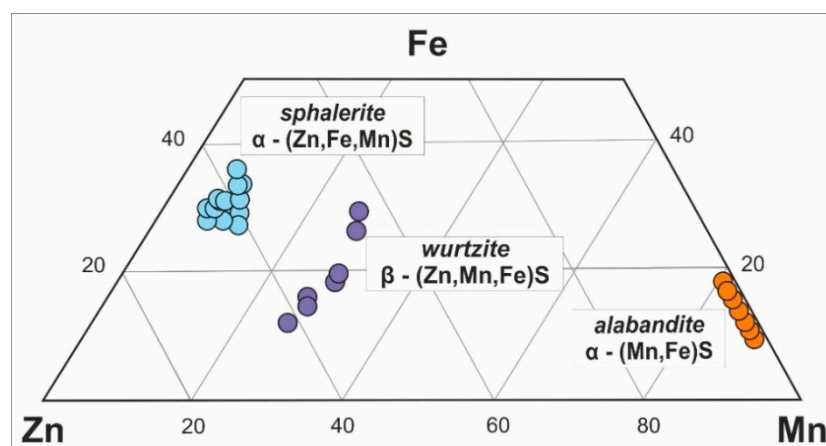


**Figure 15.** Triangular diagram in terms of atomic proportions (%) Zn, Fe, and Mn, showing the variation in wurtzite ( $n = 7$ ), sphalerite ( $n = 17$ ), and alabandite ( $n = 25$ ) compositions from the Kochumdek marbles. Based on data from Table 6. Crystal system:  $\alpha$  = isometric,  $\beta$  = hexagonal,  $n$  = number of analyses.

Sphalerite shows the ranges 17.92 to 21.87 wt% Fe and 4.01 to 7.43 wt% Mn, and the respective composition is  $\text{Zn}_{0.55-0.57}\text{Fe}_{0.32-0.35}\text{Mn}_{0.07-0.10}\text{S}$ . These values are higher for Fe but lower for Mn compared to wurtzite, which contains 7.86–19.06 wt% Fe and 16.00–18.25 wt% Mn, and has the  $\text{Zn}_{0.39-0.46}\text{Fe}_{0.19-0.31}\text{Mn}_{0.28-0.30}\text{S}$  composition (Figure 15; Table 6). LA-ICP-MS analyses of large sphalerite grains from spurrite-monticellite marbles (Zone 3) reveal high trace-element diversity. The high-Fe sphalerite (170,400–171,100 ppm) also carries significant concentrations of Mn (41,400–53,160 ppm), moderate Cd (4170–5000 ppm), fairly low Co (181–293 ppm), as well as trace amounts of Hg (50.0 ppm), In (23.0 ppm), Cu (18.1 ppm), and Se (5.73 ppm). The concentrations of Ni, Tl, Ge, Mo, Ga, Ag, Au, As, and Sb are below the detection limits. The trace-element composition of wurtzite remains uncertain because of the very small grain sizes.

Both prograde and retrograde rasvumite phases are close to  $\text{KFe}_2\text{S}_3$  (Table 9). LA-ICP-MS analysis of coarse rasvumite-I grains reveals a full scope of specific impurities: 559–815 ppm Rb, 224–858 ppm Ba, 149–293 ppm Na, 31.9–69.0 ppm Cs, and 3.64–19.8 ppm Tl, which are typical of rasvumite from different alkaline magmatic and metasomatic assemblages [67,69–72]. The contents of Mn, Zn, and Cd vary by orders of magnitude (104 to 5130 ppm, 22.1 to 1280 ppm, and 0.48 to 12.1 ppm, respectively) and show spikes due to the presence of (Mn, Fe)S and (Zn, Fe, Mn)S micro-inclusions [34]. Other trace elements are low (in ppm): Se (11.6–19.5), Ga (4.62–16.9), Te (up to 1.40) and Ag (0.16).

The rims of retrograde rasvumite-II replacing pyrrhotite were too narrow for trace-element analysis, but the impurities must be low as in prograde rasvumite-I based on the near 100% totals (Table 9). On the other hand, djerfisherite replacing rasvumite in the rims shows systematic enrichments in Ni (0.50–11.01 wt%) and Cu (0.25–5.22 wt%) (Table 10). Persistence of oxygen revealed in X-ray elemental maps of rasvumite in rims and crack-filling rasvumite-II indicates both replacements by djerfisherite and partial oxidation of late-generation rasvumite (Figure 16).

**Table 9.** Representative analyses and average compositions of rasvumite ( $KFe_2S_3$ ) from marbles of the Kochumdek contact aureole (SEM-EDS and EPMA data).

Sample	Zone 2		Zone 3				Zone 4		Zones 2–4					
	PT-104	PT-91	PT-93	PT-94	PT-97	PK-16-3	Mean ( $n = 30$ )	S	Min.	Max.				
							wt%							
K	15.22	<b>16.04</b>	15.76	15.27	<b>16.36</b>	<b>16.14</b>	15.42	15.31	15.63	15.52	15.54	0.32	15.15	16.36
Fe	45.11	<b>45.46</b>	44.92	45.20	<b>45.16</b>	<b>45.11</b>	45.57	45.32	44.84	45.08	44.98	0.37	44.34	45.62
S	38.88	<b>37.50</b>	38.80	38.90	<b>38.26</b>	<b>37.95</b>	38.86	38.97	38.76	38.68	38.84	0.56	37.50	39.71
Total	99.21	<b>99.01</b>	99.48	99.37	<b>99.78</b>	<b>99.20</b>	99.85	99.60	99.23	99.28	99.36			
							a.p.f.u.							
K	0.963	<b>1.052</b>	0.999	0.966	<b>1.052</b>	<b>1.047</b>	0.976	0.966	0.992	0.987	0.984			
Fe	1.998	<b>2.088</b>	1.994	2.001	<b>2.033</b>	<b>2.047</b>	2.020	2.003	1.992	2.007	1.994			

a.p.f.u. = atoms per formula unit. Formula based on 3 atoms of S. Na, Co, and Ni (<0.03 wt%), Cu and Rb (<0.04 wt%), and Cs (<0.08 wt%) are below detection limits for EPMA. Sample PT-104 (Zone 2)—large rasvumite grains (rasvumite-I), other samples—fine-grained secondary rasvumite (rasvumite-II); Mean = average value,  $n$  = number of analyses,  $S$  = standard deviation, Min. = minimum value, Max. = maximum value. Bold = EPMA data, other analyses performed on SEM-EDS.

**Table 10.** Representative analyses of djerfisherite ( $K_6(Fe,Ni,Co,Cu)_{25}S_{26}Cl$ ) from marbles of the Kochumdek contact aureole (EPMA data).

Sample	Zone 2				Zone 3		Zone 4		
	PT-104	PT-107		PT-97		PT-89	PK-16-3		
	wt%								
K	9.52	9.57	8.93	9.39	9.62	9.45	9.50	9.39	9.58
Fe	51.84	42.85	44.67	46.42	47.04	51.42	51.35	52.59	51.47
Ni	0.99	11.01	9.19	6.37	2.54	1.13	1.92	1.77	1.97
Co	<0.03	0.66	1.00	0.35	<0.03	<0.03	<0.03	<0.03	<0.03
Cu	0.94	0.94	1.60	1.67	5.22	1.04	1.32	<0.04	<0.04
Mn	<0.04	<0.04	<0.04	<0.04	<0.04	<0.04	<0.04	1.39	1.55
S	34.27	34.30	32.75	34.14	34.00	34.58	33.53	33.08	33.80
Cl	1.55	1.47	1.33	1.43	1.47	1.43	1.55	1.22	1.30
Total	99.11	100.80	99.47	99.77	99.89	99.05	99.17	99.44	99.67
	a.p.f.u.								
K	5.923	5.948	5.813	5.864	6.032	5.826	6.040	6.052	6.043
Fe	22.578	18.646	20.358	20.295	20.650	22.194	22.858	23.729	22.729
Ni	0.410	4.558	3.985	2.650	1.061	0.464	0.813	0.760	0.828
Co	0.000	0.272	0.432	0.145	0.000	0.000	0.000	0.000	0.000
Cu	0.360	0.359	0.641	0.642	2.014	0.395	0.516	0.000	0.000
Mn	0.000	0.000	0.000	0.000	0.000	0.000	0.000	0.638	0.698
Cl	1.063	1.008	0.955	0.985	1.017	0.972	1.087	0.867	0.904
$\Sigma$ Me	23.348	23.836	25.416	23.731	23.725	23.053	24.188	25.126	24.252

a.p.f.u. = atoms per formula unit, formula based on 26 atoms of S, Na (<0.03 wt%), Rb (<0.04 wt%), Ba and Cs (<0.08 wt%) are below detection limits,  $\Sigma$  Me = Fe + Ni + Co + Cu + Mn.

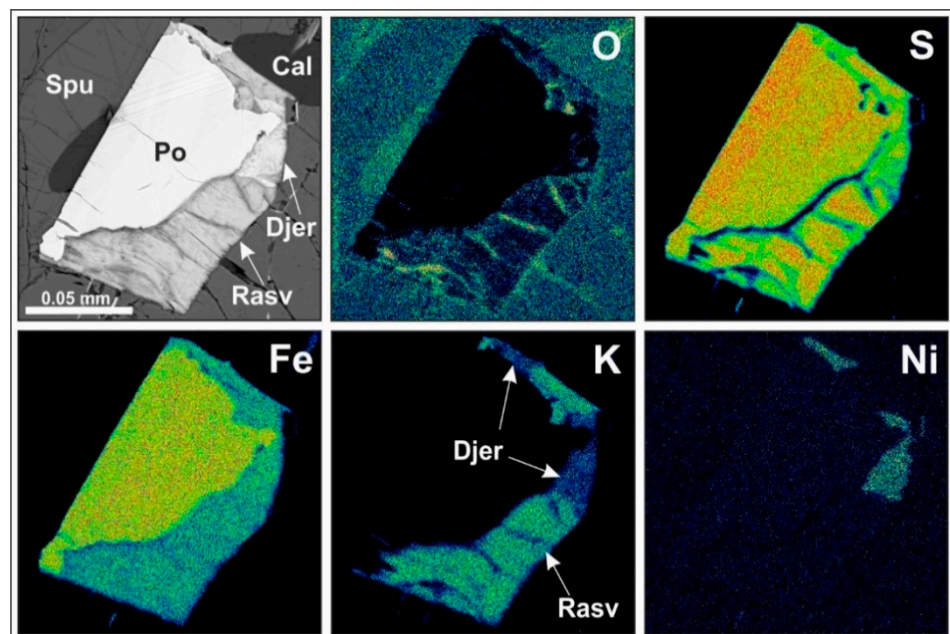


**Figure 16.** BSE image and X-ray elemental maps (O, S, Fe, K, Ni) of pyrrhotite partially replaced by rasvumite and djerfisherite. Elemental mapping revealed the constant presence of oxygen (O) in rasvumite, which indicates its partial oxidation. Kochumdek marble, Zone 2, sample PT-107. Cal = calcite, Djer = djerfisherite, Po = pyrrhotite, Rasv = rasvumite, Spu = spurrite.

Djerfisherite has a highly variable composition, with relatively constant K (8.93–9.90 wt%), Fe in a range of 42.85 to 53.51 wt%, 1.08 to 1.57 wt% Cl, 32.75 to 34.89 wt% S, and Na content below the detection limits of both SEM-EDS and EPMA techniques (Table 10). The ranges of

Ni, Cu, and Co are quite large. Coarse particles of djerfisherite are often compositionally homogeneous, though Fe, Ni, Cu, and Co contents in individual grains may differ even within half of a thin section area (Figure 17). The distribution of djerfisherite enriched or depleted in these metals shows some pattern: the contents of Ni and Co are the highest (reaching 11.01 wt% and 1.00 wt%, respectively) in djerfisherite near the sill margin in Zone 2 and the lowest (<2.00 wt% Ni and <0.01 wt% Co) 1.5 m away from the contact in Zone 4. The respective compositions are  $K_{5.81-5.95}(Fe_{18.64-22.57}Ni_{0.41-4.55}Cu_{0.35-0.64}Co_{0.0-0.43})S_{26}Cl_{0.95-1.07}$  and  $K_{6.0}(Fe_{22.46-23.72}Ni_{0.20-0.83}Mn_{0.0-0.69}Cu_{0.0-0.52}Co_{0.0})S_{26}Cl_{0.86-1.08}$ . Djerfisherite in Zone 4 also contains up to 1.55 wt% Mn and approaches the Fe-endmember composition. Copper variations are less regular and reach the maximum (5.22 wt% Cu) in djerfisherite from the marbles of Zone 3.

Another retrograde K-Fe sulfide in Zone 4, tentatively interpreted as bartonite ((K,Me<sup>2+</sup>)(Fe,Cu,Ni)<sub>25-x</sub>S<sub>26</sub>(S,Cl), tetragonal), is Cl-free and has quite a homogeneous composition: 10.10–10.38 wt% K, 45.30–51.45 wt% Fe, 0.37–3.60 wt% Ni, 0.46–1.83 wt% Cu, 0.45–0.53 wt% Co, and 37.35–38.11 wt% S ( $K_{5.82-6.08}Fe_{18.42-21.50}Ni_{0.0-1.45}Cu_{0.0-0.69}Co_{0.0-0.21}S_{27}$ ) (Table 11).

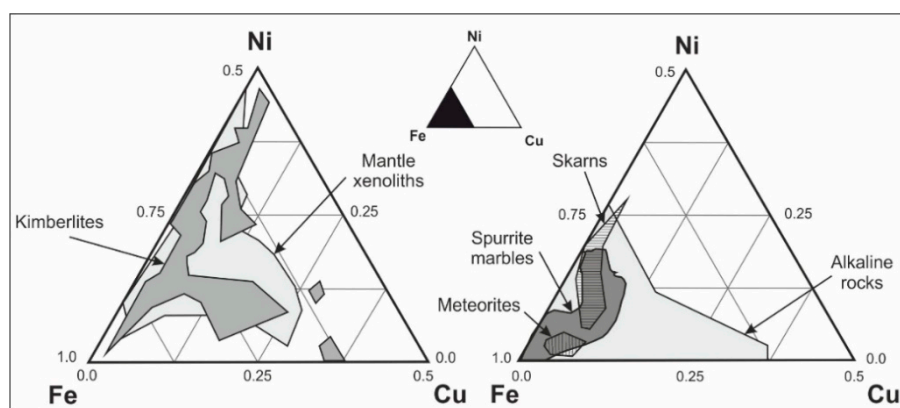


**Figure 17.** Fe–Ni–Cu diagram (at%) of djerfisherite compositions from the terrestrial rocks of various genesis and meteorites. Modified version after [31]. Based on data: mantle xenoliths [73–80], kimberlites [72,78,80,81], alkaline rocks [82–84], skarns [85], meteorites [84,86,87]. Compositional field of djerfisherite from spurrite marbles plotted using author data.

**Table 11.** Representative analyses of bartonite (K<sub>6</sub>Fe<sub>21</sub>S<sub>27</sub>) from Tly-Wo marbles (Zone 4) of the Kochumdek contact aureole (SEM-EDS data).

Element	Sample						
	PT-88		PT-91		PK-16-1		
	wt%						
K	10.10	10.38	10.19	10.33	10.26	10.14	10.28
Fe	47.04	47.12	46.31	45.30	51.45	50.80	50.04
Ni	2.45	2.48	3.03	3.33	<0.30	<0.30	0.48
Co	0.53	0.52	0.50	0.49	<0.30	<0.30	<0.30
Cu	1.43	1.68	1.68	1.69	<0.30	0.46	0.71
S	37.56	38.03	37.57	38.11	37.35	37.64	38.12
Total	99.11	100.21	99.28	99.25	99.06	99.04	99.63
	a.p.f.u.						
K	5.953	6.043	6.005	6.001	6.082	5.964	5.971
Fe	19.414	19.205	19.106	18.424	21.351	20.919	20.347
Ni	0.962	0.962	1.188	1.289	0.000	0.000	0.186
Co	0.207	0.201	0.195	0.189	0.000	0.000	0.000
Cu	0.519	0.602	0.609	0.604	0.000	0.166	0.254
Σ Me	21.100	20.969	21.100	20.506	21.351	21.086	20.787

a.p.f.u. = atoms per formula unit, formula based on 27 atoms of S; Na, Ba, Rb, Cs, Mn < 0.30 wt%; Σ Me = Fe + Ni + Co + Cu. Tly = tilleyite, Wo = wollastonite.

#### 4.4. Stable Sulfur Isotopes in Pyrrhotite

The sulfur isotope composition was analyzed in hand-picked pyrrhotite fractions selected from the Kochumdek gabbro, marly limestone, recrystallized limestone (Zone 5), and marble (Zones 2 and 4) samples (Table 12; Figure 18). Pyrrhotite from both parent and recrystallized limestones has the lightest sulfur isotope composition with a narrow  $\delta^{34}\text{S}$  range of  $-28.68$  to  $-23.32\text{‰}$  corresponding to common S-bearing organic matter of marine anoxic sediments [88]. Pyrrhotite from marbles is likewise depleted in  $^{34}\text{S}$ , with  $\delta^{34}\text{S}$  in the  $-25.36$  to  $-25.18\text{‰}$  range in Zone 2 and slightly less negative  $\delta^{34}\text{S}$  values in Zone 4 ( $-15.07\text{‰}$ ). Pyrrhotite from gabbro has positive  $\delta^{34}\text{S}$  from  $+2.68$  to  $+13.10\text{‰}$ , which can be a sign of different scale contamination of mantle-derived basic sulfides ( $\sim 0\text{‰}$ ) with evaporitic sulfate ( $\delta^{34}\text{S}$  about  $+20\text{‰}$ ) derived from seawater [88,89].

**Table 12.** Sulfur isotope compositions of pyrrhotite from recrystallized marly limestones and marbles from the Kochumdek contact aureole, and gabbro from the Kochumdek trap, compared with stratotype marly limestone of the Lower Kochumdek Sub-formation.

Sample	Rock Type	$\delta^{34}\text{S}$ (CDT) $\text{‰}$
PK-16-5 *	Marly limestone	$-28.25 \pm 0.20$
PK-2	Recrystallized marly limestone	$-26.75 \pm 0.20$
PK-3-2	Recrystallized marly limestone	$-27.62 \pm 0.20$
PK-3-3	Recrystallized marly limestone	$-25.84 \pm 0.20$
PK-4-7	Recrystallized marly limestone	$-28.68 \pm 0.20$
PK-6-1	Recrystallized marly limestone	$-23.32 \pm 0.20$
PK-12-1	Tly-Wo marble (Zone 4)	$-15.07 \pm 0.20$
PT-117	Mw-Spu marble (Zone 2)	$-25.18 \pm 0.20$
PT-122	Mw-Spu marble (Zone 2)	$-25.36 \pm 0.20$
PT-95	Gabbro	$+13.10 \pm 0.20$
PK-9-2	Gabbro	$+2.68 \pm 0.20$
PK-17-4	Gabbro	$+3.31 \pm 0.20$

\* = stratotype marly limestone of the Lower Kochumdek Sub-formation. Mw = merwinite, Spu = spurrite, Tly = tilleyite, Wo = wollastonite.

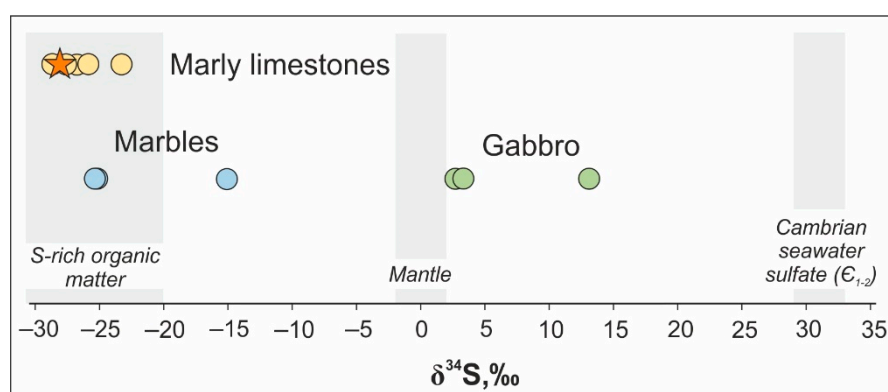


**Figure 18.** Sulphur isotope composition of sulfides (mainly pyrrhotite) from recrystallized marly limestones, marbles and gabbro from the Kochumdek contact aureole in comparison with stratotype marly limestone of the Lower Kochumdek Sub-formation (orange star) (based on data from Table 12) and with data for S-rich organic matter after [88], mantle after [28], and Cambrian seawater sulfate after [90].

## 5. Discussion

### 5.1. General Geochemical Features of Adjacent Igneous and Sedimentary Rocks

The limestones of the Tunguska basin underwent intense phase changes upon interaction with the high temperature (at least  $1200\text{ °C}$  [30]) mafic magma intrusion during



the Early Triassic. High temperature spurrite-merwinite metamorphism was restricted to a narrow zone within 2.5–3 m away from the contact. The top of the Kochumdek sill bears no evidence of auto-metasomatism or vein mineralization, while both the contact and interior parts of marbles lack breccias or vein stockworks, and skarns are limited to a 3 cm thick discontinuous zone. In general, the local geology of the aureole records a regime of thermal metamorphism close to an ideal model of isochemical transformations with only a minor role of metasomatic agents. In order to find out how much the natural process matched the model and why such exceptional conditions arose in the Kochumdek aureole, we compared the geochemical features of the rocks and studied the composition and distribution of sulfide mineralization.

The contrasting trace-element compositions of the Kochumdek limestone and igneous samples allow for the use of geochemical tracers to decipher the fluid flow patterns in the contact area by estimating the relative extent of the fluid flow, as well as the distribution of sulfide minerals as carriers of fluid components. The Cr, Ni, Co, Cu, V, Sc and Cl inputs and isotopically heavy sulfur would have left an imprint on the marbles if they were affected by metasomatic fluids released from the cooling igneous body. However, no such signatures of element transport would exist in the case of isochemical contact metamorphism. We focused the study on sulfides in the aureole rocks, largely due to their diversity where in addition to ubiquitous pyrrhotite, the sulfide assemblage includes numerous rare phases, each being a potential proxy of growth conditions. Another reason is that sulfides are sensitive to re-crystallization and re-equilibrate promptly in response to changes in the growth medium.

The interaction between the gabbro from the top of the Kochumdek sill and marly limestones exhibits a number of informative geochemical and mineralogical fingerprints. The Kochumdek gabbro samples correspond to intraplate basalts according to mineralogy, bulk-rock chemistry and trace-element composition [42,91]. They are marked by Fe-, Ti-, V- and Sc-enrichments, moderate-to-low Cr, Ni, Co, and Cu contents, and low concentrations of S, Mn, and Zn. Apatite-group minerals and late phases in the gabbro contain appreciable amounts of chlorine but lack sulfate sulfur, which is an indication of low oxygen fugacity in the crystallizing melt [21]. The same conditions, as well as the redox regime of cooling basaltic magma, controlled the accessory mineral assemblage. Magnetite, common to these rocks, is enriched in Ti and V and coexists with ilmenite. Sulfide mineralization is scarce (Fe, Cu, Ni, and Co sulfides), where pyrrhotite is predominant and enriched in Ni, Co, and Se, depleted in Mn, and contains trace amounts of Mo and Ag (Table 8; Figure 14). Pyrrhotite from the gabbro is defined by  $\delta^{34}\text{S}$  from +2.68‰ to +13.10‰, which differs significantly from the isotopically light sulfur in sulfides from the Lower Silurian limestones and marbles (Figure 18; Table 12).

The variable and higher  $\delta^{34}\text{S}$  of igneous rocks in the Tunguska basin can be attributed to contamination of basaltic magma with Ordovician limestones that bear gypsum and/or anhydrite with high  $\delta^{34}\text{S}$  values (+21.0 to +32.2‰) [92] or Middle and Early Cambrian evaporates ( $\delta^{34}\text{S}$  from +9 to +2‰). The latter effect is especially prominent in the Norilsk area in the northern flank of the basin [28,68,93].

Intact and recrystallized marly limestones are depleted in Cr, Ni, Co, Cu, V, and Sc relative to the gabbro samples, but are notably more enriched in isotopically light sulfur and Mn, and occasionally show positive Zn spikes (Table 8; Figure 14). Their accessory authigenic mineralization is largely composed of pyrite (originally As-enriched, typical of marine anoxic sediments [94–96], As-bearing pyrrhotite, arsenopyrite, as well as unevenly distributed galena and sphalerite.

## 5.2. Sulfides in High-Grade Contact-Metamorphic Marbles: Applicability to Thermal History Reconstructions

### 5.2.1. Matrix and Inclusion Sulfides

The mineralogy of sulfides and in particular, exsolution textures, are of broad use as a proxy for reconstructing the cooling history of meteorites [87]. Multiphase and multistage sulfide assemblages have been documented extensively in skarn deposits [26]. However,

little is known of the difference between inclusion and matrix sulfide assemblages in contact metamorphic rocks. In this respect, the zoned Kochumdek aureole may be an advantageous test site, as it appears to have undergone a relatively simple set of events and mainly quasi-isochemical metamorphism. There are several key features known about the aureole which render it a suitable reference: (i) the exact intrusion body, which triggered thermal alteration of sediments, (ii) the sedimentary precursor rocks, (iii) there was a single thermal event, and (iv) there are numerical constraints on the duration of heating in each metamorphic zone [1,2,29,30].

The features and timing relationships of sulfides and their assemblages in the Kochumdek marbles are interpreted following the ideology of Brown et al. (2014) [27]. Sulfide inclusions in prograde rock-forming minerals are considered to be isolated and thus unmodified by subsequent retrograde fluid-mineral interactions. Monomineralic inclusions are considered to be relics of peak metamorphic conditions (except for possible polymorphic transformations). They reflect the scope of the respective solid solutions and the trace-element peculiarity of individual minerals which were stable under those conditions. Polyphase sulfide assemblages within a single inclusion are either intergrowths of syngenetic high-temperature phases or decomposition products of complex precursors which broke down upon cooling. The main isochemical changes in response to temperature drop, with no reaction between sulfide phases, include: (i) polymorphic transformations, (ii) exsolution (compositional change of solid solutions), and (iii) the breakdown of high-temperature stoichiometric phases to multiphase assemblages of the same overall bulk compositions but different stoichiometry for each newly formed phase [27]. As a consequence, the sulfide assemblages occurring as inclusions may be different from those originally incorporated under the peak temperature conditions [97]. However, the bulk chemistry of such multiphase inclusions also remains invariable and provides information about sulfides that existed at the time of their entrapment by crystallizing prograde rock-forming minerals [27].

The sulfide inclusions surrounded by tiny cracks or connected via radial cracks with the matrix were exposed to retrogressive fluids and can be classified as pseudo-inclusions [27]. Their compositional difference from true (i.e., isolated) inclusions provides insights into some of the peculiarities of retrogressive fluids (e.g., sulfur activity, major-ion chemistry and oxygen fugacity patterns).

In long-lived metamorphic complexes in subduction zones, the common and large matrix sulfides are considered to be late-stage phases that formed after (possibly long after) the prograde sulfides were trapped as true inclusions [27], and the two groups of sulfide assemblages often show systematic differences. Matrix sulfides commonly form by transformation, replacement or alteration of their higher-grade precursors, but may also result from delayed re-incorporation of sulfur into the metamorphic rocks via cracks or any other lithological heterogeneities. The small-scale fluid pathways increase rock permeability and control the precipitation of new sulfide minerals. Major- and trace-element patterns of early and late sulfide phases, as well as their sulfur isotopic composition, have implications for the source(s) of fluids, metals, and sulfur, and thus can provide insights into the history of metamorphic rocks [26,27,98,99].

Crack-filling sulfides and minerals that rimmed and/or replaced earlier sulfides are attributed to the oldest retrogressive events. They may form long after both inclusion and matrix sulfides or follow immediately as a response to temperature and pressure drop.

The recrystallized limestones of the Kochumdek aureole retain all geochemical features of their sedimentary precursors and bear monotonic sulfide mineralization, with predominantly pyrrhotite, which has a negative  $\delta^{34}\text{S}$  values ( $-28.68\text{‰}$  to  $-23.32\text{‰}$ ) and contains Mn, Ni, and Co impurities, as well as trace amounts of Se (Figures 14 and 18; Tables 8 and 12). The morphology of pyrrhotite provides a strong indication that it formed by integrative recrystallization (Figure 10B,C). Chalcopyrite, galena and arsenopyrite occur sporadically, mainly as fine inclusions on the periphery of pyrrhotite grains, and thus most likely record the removal of impurities from the precursor pyrite and/or pyrrhotite during recrystallization. The sulfides in marbles from Zone 4 also include rare grains of acanthite

and alabandite. Sulfides occur mostly in the matrix, except for a few pyrrhotite inclusions in calcite. Thus, the composition of sulfide inclusions in low-grade rocks is distinct from matrix minerals, where Fe-sulfides are predominant, while matrix pyrrhotite coexists with Mn, Ag, and Pb sulfides.

The merwinite- and spurrite-monticellite marbles of Zones 2 and 3 demonstrate geochemical inheritance from the protolith sediments, and their bulk trace-element compositions lack any notable signatures of material transport from the sill. The marbles show moderate enrichment in Mn and Zn and preserve low contents of Cu ( $\leq 60$  ppm), Ni ( $\leq 30$  ppm), and Co ( $\leq 15$  ppm) (Table 3). However, sulfide assemblages in merwinite marbles differ from their counterparts from both lower-grade zones and precursor sediments in terms of greater compositional diversity (Fe, Mn, Zn, Pb, and Ag sulfides) and in similarity of inclusion and matrix sulfide assemblages.

The trace-element composition and isotopic signatures of pyrrhotite provide convincing evidence for the isochemical nature of high-temperature metamorphism in the Kochumdek aureole. Matrix pyrrhotite from merwinite assemblages were analyzed by LA-ICP-MS, and monofraction samples were selected from the same assemblages for sulfur isotope analysis. Hypothetically, sulfides from the matrix (unlike those of inclusions) would be better candidates for recrystallization by fluids released from the cooling magma. If this were the case, they would store geochemical fingerprints of mafic magma, such as Ni, Co, and Cu enrichment, as well as reintroduced isotopically heavy sulfur, especially in pyrrhotite from the merwinite zone. However, matrix pyrrhotite from merwinite marble is strongly depleted in Ni, Co, Cu, Se, Mo, and Ag and has  $\delta^{34}\text{S}$  values about  $-25\%$  (Figures 14 and 18; Tables 8 and 12).

The obtained results show the compositional features of ultrahigh-temperature sulfides occurring under spurrite-merwinite facies conditions during thermal alteration of marly limestone, which so far has only been achieved for sphalerite from combustion metamorphic rocks [53]. Iron is the principal mineral-forming cation in the Kochumdek marble and, together with Mn, is among main components in the  $(\text{Zn,Fe,Mn})\text{S}_{\text{cub}}$ ,  $(\text{Zn,Mn,Fe})\text{S}_{\text{hex}}$ , and  $(\text{Mn,Fe})\text{S}_{\text{cub}}$  solid-solution series, which coexists with the predominant pyrrhotite.

Alabandite ( $\alpha$ -(Mn,Fe)S) is the only proper Mn phase in the Kochumdek marbles. Its origin is likely attributable to: (i) markedly higher bulk contents of Mn than Zn in the sedimentary protoliths, and to (ii) restricted storage capacity of pyrrhotite structure with respect to  $\text{Mn}^{2+}$  [65]. The combined action of the two factors prevented total Mn dissemination in the (Fe,Mn)S or (Zn,Fe,Mn)S solid solutions. It is possible that  $\alpha$ -(Mn,Fe)S formed as a primary high-temperature phase, judging by its presence as inclusions in the rock-forming minerals from spurrite marbles (Figure 11). On the other hand, the systematic coexistence of fine and very fine (Mn,Fe)S particles on the boundary of larger pyrrhotite grains (both inclusions and matrix) indicates that (Mn,Fe)S may have also separated during high-temperature purification of pyrrhotite. The latter hypothesis is supported by direct comparison of impurities in pyrrhotite from different metamorphic zones (Figure 14), where the Mn contents are the highest in pyrrhotite from Zone 4 but low at the top of the sill. The Mn depletion rules out any notable transfer between the magma and limestone/marble material, and magma contamination by the latter.

The actual process of Mn fractionation may have been much more complicated. It is pertinent to note that Mn impurities occur in all Fe-bearing minerals from the Kochumdek marbles. The amount of Mn in rock-forming Ca-Mg silicates increases proportionally with increasing Mg:Ca ratio, and peaks at  $\approx 3$  wt% MnO in monticellite  $\text{Ca}(\text{Mg}_{0.59-0.82}\text{Fe}_{0.12-0.26}\text{Mn}_{0.03-0.07})(\text{SiO}_4)$  [30,61]. Manganese is present in magnetite rims around pyrrhotite (1.33–6.77 wt% MnO) but is absent from all Ca minerals (calcite, tilleyite, spurrite, rankinite). Its contents are below the detection limit even in wollastonite, which is known to readily incorporate Mg, Fe and Mn at high temperatures [100]. Tiny inclusions of Zn(Fe-Mn) and Mn(Fe) sulfides were commonly found trapped in melilite and might be interpreted as a consequence of Fe uptake during the growth of complex silicates. Less often, such inclusions are found in Fe- and Mn-free spurrite, but are absent in monticellite

which is the main Fe and Mn host silicate phase in the Kochumdek marble. This provides evidence for efficient crystallochemical fractionation of Mn during ultrahigh-temperature low-pressure contact metamorphism, as well as for strong Fe-Mn coupling.

The solid solution series  $(\text{Zn,Fe,Mn})\text{S}_{\text{cub}}$ ,  $(\text{Zn,Mn,Fe})\text{S}_{\text{hex}}$ , and  $(\text{Mn,Fe})\text{S}_{\text{cub}}$  has preserved unusual compositions consistent with equilibration at near extreme temperatures and thus may have grown at peak metamorphic conditions. Although the rapid kinetics of re-equilibration under cooling in sulfides [24] limits their use as geothermometers, they can yield some threshold estimates. At high temperatures, Fe and Mn can more easily incorporate into both sphalerite and wurtzite structural types [64,101]. Sphalerite from the ultrahigh-temperature merwinite marbles of the Kochumdek aureole contains about 20 wt% Fe on average and up to 5.9 wt% Mn, while Zn is below 0.6 atoms per formula unit (a.p.f.u.) ( $\text{Zn}_{0.55-0.57}\text{Fe}_{0.32-0.35}\text{Mn}_{0.07-0.10}\text{S}$ ). The minerals appear homogeneous and free from exsolution lamellae under SEM magnification (up to 0.5  $\mu\text{m}$ ), but intergrowths might exist on the submicron scale. In the natural environment, iron reaches the highest contents (25.3–32.1 wt% Fe or 42–50 mol% FeS) in sphalerite from meteorites which form at temperatures above 900 °C (1200 K) [87]. Experiments show that FeS in  $(\text{Zn,Fe})\text{S}_{\text{cub}}$  ranges from 20 to 55 mol% at 850 °C, but its content in  $(\text{Zn,Fe})\text{S}_{\text{cub}}$  equilibrated with pyrrhotite decreases to  $\leq 13$  mol% as the temperature drops to 742 °C at 1 bar [26].

The incorporation of large amounts of Mn stabilizes the wurtzite-type structure [101]. In the analyzed samples, wurtzite occurs only as inclusions in melilite from merwinite assemblages and contains comparable concentrations of Fe (12.0 to 19.1 wt%) and Mn (16.8 to 18.3 wt%), and anomalously low Zn ( $\text{Zn}_{0.39-0.46}\text{Fe}_{0.19-0.31}\text{Mn}_{0.28-0.30}\text{S}$ ). According to experimental evidence [102], synthesis of Mn-rich wurtzite is possible at temperatures no lower than 800 °C. The wurtzite inclusions are rare in the Kochumdek marbles and occur in coarse pyrrhotite grains. Therefore, it remains unclear whether they originated simultaneously with predominant pyrrhotite at the peak conditions or were separated while pyrrhotite was expelling Mn and Zn impurities.

Alabandite ( $\text{MnS}_{\text{cub}}$  or  $\alpha\text{-MnS}$ ) belongs to the galena (or NaCl) structural type and the  $(\text{Mn,Fe})\text{S}_{\text{cub}}$  solid solution is more restricted than  $(\text{Zn,Fe})\text{S}_{\text{cub}}$  [65]. The MnS-FeS solid solutions in the Kochumdek marbles contain up to 15.7 wt% or 0.25 a.p.f.u. Fe ( $\text{Mn}_{0.76-0.89}\text{Fe}_{0.12-0.25}\text{S}$ ) (Table 6), or above the Fe-content in  $\alpha\text{-(Mn,Fe)S}$  from meteorites [87]. This is the highest amount reported for  $\alpha\text{-(Mn,Fe)S}$  ( $\text{Mn}_{0.81}\text{Fe}_{0.19}\text{S}$ ) crystals synthesized by the gas-transport method in the Fe-Mn-Zn-S system at temperatures ranging from 900 to 800 °C [103]. According to [26], the FeS-MnS solid solution has the highest miscibility in the NaCl structure at 800 °C. Unfortunately, the alabandite compositions are unsuitable for subtler temperature reconstructions and in the FeS-MnS diagram [102] they fall into the broad stability field (1300–600 °C) of the alabandite + pyrrhotite assemblage (Figure 19).

The presence of large rasvumite-I grains with perfect cleavage in the matrix of the highest-temperature merwinite marbles is intriguing, as rasvumite coexisting with pyrrhotite (in the absence of pyrite) provides a record of increasing activity of potassium and decreasing fugacity of sulfur in the mineral-forming medium [104–106]. In the context of our results, sulfur fugacity may decrease because most of the isotopically light sulfur derived from the authigenic pyrite and S-bearing organic matter of sedimentary protoliths became immobilized in the earliest ultrahigh-temperature metamorphic sulfides, mainly pyrrhotite (+ $(\text{Zn,Fe,Mn})\text{S}$  and  $(\text{Mn,Fe})\text{S}$  solid solutions). As for the greater potential of K at peak metamorphic conditions, it may result from crystallochemical fractionation because no ultrahigh-temperature Ca or Ca-Mg minerals contain K. The K-content is below the detection limit of EPMA ( $<0.02$  wt%  $\text{K}_2\text{O}$ ), even in gehlenite-rich melilite which is the only potential K host among rock-forming minerals [30,61]. Currently, there is no information on the thermal stability of  $\text{KFe}_2\text{S}_3$  phase(s). Based on isostructural with rasvumite ( $\text{KFe}_2\text{S}_3$ , space group  $Cmcm$ ) fibrous thioferrates  $\text{RbFe}_2\text{S}_3$  and  $\text{CsFe}_2\text{S}_3$  obtained by pyro-synthesis at 950 °C, ambient pressure and flowing nitrogen [107], rasvumite having shorter and stronger K-S bonds than both Rb-S and Cs-S bonds, could be stable at higher T than 950 °C.

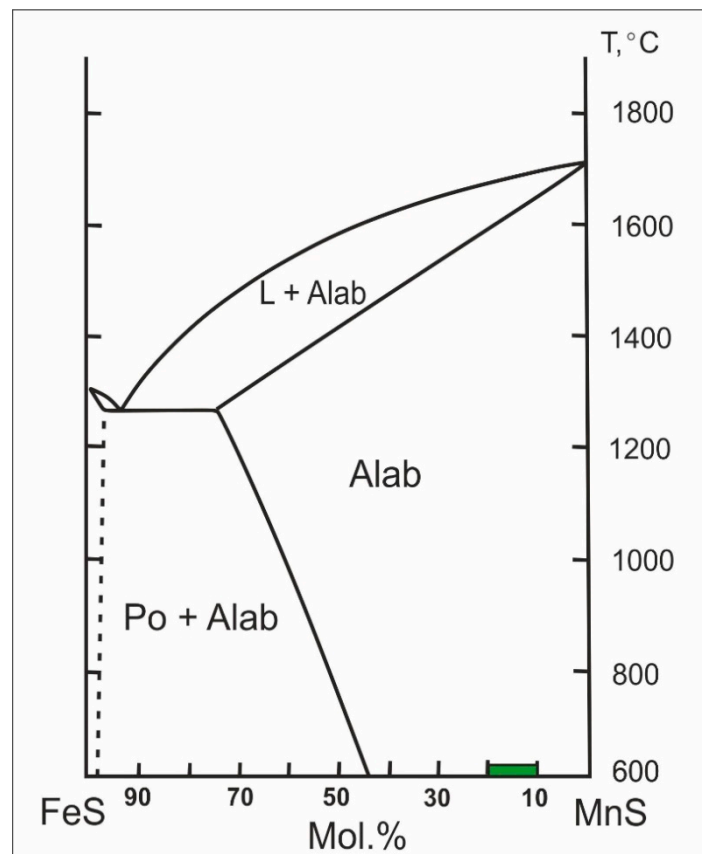


**Figure 19.** The FeS-MnS equilibrium diagram [102]. Compositional field of alabandite from spurrite marbles (green field) plotted using author data. Alab = alabandite, L = liquid, Po = pyrrhotite.

Large crystals of rasvumite-I were analyzed by SEM and LA-ICP-MS only, while direct structural determination was not possible. Meanwhile, this phase is morphologically different from needle-like rasvumite-II, and the angle between its cleavage directions, which are prominent in coarse grains, is 60 or 120° rather than 90° (perfect cleavage on {110} for orthorhombic rasvumite) (Figure 12G,H). Therefore, the merwinite assemblages of the Kochumdek marbles include a previously unknown high-temperature modification of  $\text{KFe}_2\text{S}_3$ . In addition to orthorhombic rasvumite ( $\text{KFe}_2\text{S}_3$ , space group *Cmcm*), at least two other polymorphic modifications have been synthesized so far: monoclinic  $\text{KFe}_2\text{S}_3$  (*C2/m*) [108] and low-temperature  $\text{KFe}_2\text{Se}_3$  and  $\text{RbFe}_2\text{S}_3$  phases that belong to another orthorhombic group, which break down above 450 °C [109].

### 5.2.2. Crack-Filling (Retrograde) Sulfides

The temperature constraints for the cooling of marbles can be used to reconstruct the thermal stability limits of crack-filling sulfides. Mineral assemblages in cracks differ drastically from those in both matrix and inclusions and consist of relatively abundant doublet or trio K-Fe sulfides, rasvumite + djerfisherite ± bartonite. Their ubiquity is unanticipated for K-poor calcareous rocks, even more so that such mineralization is absent from gabbro containing up to 1.4 wt%  $\text{K}_2\text{O}$  (Tables 1–3). The first reconstruction of the thermal history and some chemical parameters of the retrogression processes in the Kochumdek aureole became possible with reference to recently published experimental results on the stability limits of various Fe and K sulfide assemblages and individual compounds [105,106,110]. Pyrite-bearing mineral assemblages (pyrrhotite + pyrite + rasvumite + sylvite) and pyrite-free assemblages (pyrrhotite + rasvumite + sylvite +  $\text{KFeS}_2$ ) are stable below and above 513 °C, respectively. The absence of pyrite in the sampled marbles indicates that rasvumite replaced pyrrhotite (forming rims and pseudo-inclusions) at temperatures above 513 °C.

The exposed rocks also lack both KCl and  $KFeS_2$  phases because the former is highly soluble, while the latter is prone to hydrolysis.

The assemblage of pyrrhotite + rasvumite + djerfisherite fills cracks in marbles, as well as in recrystallized limestones. The same assemblage, plus a KCl phase (sylvite), was synthesized at 400 °C, but turned out to be unstable at 600 °C [110]. Djerfisherite was shown to melt at ambient pressure and temperatures slightly below 600 °C, where a new phase of unknown composition formed [110]. Systems of tiny cracks formed almost contemporaneously along grain boundaries in the minerals of marble and recrystallized marly limestone grains within a narrow ( $\leq 3.5$  m) zone of heating around the cooling intrusion, apparently due to differences in thermal expansion coefficients of the phases in contact. The assemblages of silicates in pelitic limestone layers constrain the heating temperatures to within 450–500 °C (Figure 4A), which appears to be the upper limit of djerfisherite formation in the aureole rocks.

Djerfisherite that replaces rasvumite-II in cracks is the only phase in the Kochumdek marbles which bears Ni, Cu, Co and Cl typical of gabbro. Its stability is controlled by the lower activity of sulfur (relative to rasvumite) and higher activity of chlorine in the fluid phase [67,72,74,80,104]. The distribution of djerfisherite in the Kochumdek marbles highlights the patterns of the magma-derived fluid flow and permeability in the cooling aureole. The localization of djerfisherite within the metapelitic layers reflects the permeability difference between calcite and Ca-Mg silicate layers. This effect was reference from sites of contact metamorphism in carbonate-silicate sequences where pure calcite (meta-carbonate) rocks act as aquitards while metapelitic layers can channel the fluid flow. Consequently, material transport is aligned with layering rather than being isotropic, and the silicate layers show distinct signatures of metasomatic alteration, mineral replacement and/or isotopic resetting [111]. In the case of Kochumdek, neither the calcite layers were infiltrated nor became the silicate layers affected by Si, Al, Mg and Fe metasomatism or S isotopic resetting of high-temperature sulfides. Therefore, there was no significant flux of material from the sill into the marly limestone. The aureole rocks were cracked only during the final stage of the event, and the deformation was restricted to micrometer-size weak zones along grain boundaries or, less often, produced tiny cracks in minerals (Figures 11 and 16). A few healed micrometer cracks contain sporadic  $\leq 10$   $\mu$ m grains of Sc-rich garnet, besides djerfisherite (Table 2), which provides additional evidence for restricted upward fluid flow from the Sc-enriched sill into the cooling country rocks.

The filling of *tiny* cracks, fissures or voids in the marble minerals and at grain boundaries consists of retrograde mineral assemblages, which are of limited abundance in the Kochumdek rocks. These assemblages record minor fluid flow in the aureole and limited heterogeneous permeability of the marbles during cooling. The formation conditions of the fluid flow can be inferred from the presence of K-Fe sulfides, especially, djerfisherite. It is no longer an apparent rare phase due to high-resolution techniques that can detect it in numerous silica undersaturated lithologies, which include alkaline ultramafic, basic and syenitic complexes and related metasomatic rocks [82–84]; kimberlites, kimberlite-hosted mantle xenoliths, and carbonatites, where djerfisherite is frequently localized at sites of NaCl and KCl or in Cl-bearing nodules [33,72,78–81]; mafic intrusions, with mainly Cu or Ni djerfisherite varieties [83,112]; skarns, where its presence is commonly attributed to infiltration of K- and Cl-bearing fluids from plutons [113–115]; and in few contact-metamorphic marble settings akin to Kochumdek [69]. The formation of djerfisherite in the Kochumdek marbles, which are depleted in K and Cl and have sedimentary protoliths devoid of evaporates [48], could be attributed to external fluids enriched in both K and Cl.

Studies of infiltration patterns and phase composition changes in fluids from cooling contact aureoles [49,116] demonstrate that brines should release inevitably from the fluids at temperatures below the second critical point. For the case of impure marbles with thin calcareous argillic bands (Bufa del Diente contact aureole, Mexico), these authors showed that  $CO_2$ -rich fluid produced by decarbonation of limestone escaped as an immiscible low-density  $CO_2$ - $H_2O$  fluid (with  $X_{CO_2} \geq 0.5$ ). According to the suggested model [49,116],

light internal fluid leaves its parent rock and rises into the overlying strata via grain-edge flow, while the residual lower-temperature evolved fluid (mainly external hypersaline (Na-K-Cl) brine of magmatic origin) becomes locked in metapelite layers which acts as a contact-metamorphic aquifer, unlike the largely impervious thick-bedded pure calcite marble acting as a specific aquitard.

The cooling marbles of the Kochumdek aureole were infiltrated by externally-derived saline fluids (with Ni, Co, Cl and Sc tracers) that separated from crystallizing magma. Modest amounts of such fluids can be inferred from low fluid saturation of poorly differentiated bodies of the Kuz'movskiy complex, which is consistent with the absence of skarns within the aureole. The mechanically strong massive marbles in the contact zone acted as an aquitard, while highly restricted penetration of brines and their migration via silicate layers was only possible through a system of small cracks that formed during the cooling. The fluid distribution pattern and the limited scale of the event are evident from the distribution of djerfisherite in SEM elemental maps (Figure 12B,E and Figure 16).

## 6. Conclusions

1. The Kochumdek aureole of spurrite-merwinite marbles, though being almost free of skarn features, is a locality with an exceptional diversity of sulfide minerals (fifteen mineral species). The chemical difference of sulfides from marbles (Fe,K,Mn,Zn,Pb,Ag) and gabbro (Fe,Ni,Cu,Co), as well as contrasting  $\delta^{34}\text{S}$  values, indicate that the high-temperature (750–900 °C) contact metamorphism of marly limestone was nearly isochemical, without transport of isotopically heavy sulfur and metals (Cu,Ni,Co) across the gabbro-sediment interface. Such transport was impeded by limited amounts of fluid in the igneous body, as well as the massive structure of the host marly limestone which was originally free from weak zones as potential fluid conduits and thus acted as a specific aquitard during the brief period of prograde metamorphism.

2. The data on studied sulfides have implications for the conditions of spurrite-merwinite metamorphism. Broad solid solutions of  $(\text{Zn,Fe,Mn})\text{S}_{\text{cub}}$  and  $\alpha\text{-(Mn,Fe)S}$ , as well as the discovery of a (Mn,Fe)-rich wurtzite in the Kochumdek marbles, record unusually high peak temperatures of metamorphism at the intrusion contact to at least 850–900 °C. These temperature estimates, mainly from matrix sulfide data, are consistent with those based on silicate mineral assemblages [30]. Based on the similarity of sulfide assemblages in the matrix and in the inclusions, along with the compositional similarity of individual minerals, these texturally different sulfide assemblages in high-grade zones formed within a short time under comparable temperatures. According to numerical constraints [30], the hottest conditions ( $T \geq 830$  °C) near the intrusion margins (Zone 2 or merwinite marbles) were maintained for six to eight months. This brief thermal event has changed the micritic marly limestone into quite coarse marble. The similarity of the matrix and inclusion sulfide assemblages may be attributed to the brevity of geological processes. Restricted infiltration of magma-derived saline fluids (with specific Ni, Co, Cu and Sc geochemistry) took place during retrogression and led to the formation of crack-filling assemblages of K-Fe sulfides with sporadic Sc-garnet.

3. LA-ICP-MS examination of pyrrhotite, sphalerite, and rasvumite has provided the first evidence that spurrite-merwinite metamorphism of a carbonate protolith can induce crystallochemical fractionation and accumulation of chalcophile (Ni, Cu, Co, Zn, Mn, Cd, Tl, Hg, In, Se), as well as some incompatible large-ion (Rb, Cs, Ba) elements. Under the peak temperature ( $T > 900$  °C), the majority of iron was incorporated into the pyrrhotite and sphalerite structural types, but only small amounts incorporated into the galena structural type, whereas Mn became preferably concentrated in the galena and wurtzite structural types. The selective accumulation of other elements was: Rb, Cs, Tl, Ba and Se in the  $\text{KFe}_2\text{S}_3$  phase (Rasv-I); Cd, In, and Hg in sphalerite; and Ni and Co in pyrrhotite.

**Author Contributions:** Project idea: E.V.S., A.S.D. and S.N.K.; Mineralogy and petrography: A.S.D., E.V.S. and S.N.K.; Field work: E.V.S.; Geochemistry: E.V.S., A.S.D., K.A.P., S.N.K., and D.A.A.; SEM analyses: A.S.D. and E.V.S.; EPMA analyses: A.S.D. and E.V.S.; LA-ICP-MS analysis: D.A.A. and

E.V.S.; ICP-MS analysis: K.A.P.; Sulfur isotope analysis: A.A. and V.N.R.; Interpretation of analytical data: A.S.D., E.V.S., S.N.K. and V.N.R.; Visualization: A.S.D., and S.N.K.; Writing: E.V.S., A.S.D., S.N.K., V.N.R. and A.A. All authors have read and agreed to the published version of the manuscript.

**Funding:** The reported study was funded by RFBR according to the research project No. 20-05-00216. The study was realized under the state assignment of IGM SB RAS.

**Institutional Review Board Statement:** Not applicable.

**Informed Consent Statement:** Not applicable.

**Data Availability Statement:** The data set is presented directly in the present study. Additional data (unpublished) are available upon request from the corresponding author (A.S.D.).

**Acknowledgments:** We thank the anonymous reviewers for their valuable comments, which we accepted with gratitude. We wish to thank E.N. Nigmatulina, M.V. Khlestov P.V., and T.I. Perepelova (IGM, Novosibirsk) for helpful advice. Our colleagues O.P. Polyansky, P.V. Khvorov, and A.V. Babichev (IGM, Novosibirsk) are acknowledged for their help in the field work (2017). We wish to thank V.V. Reverdatto and V.Yu. Kolobov who first visited the study object (1960 and 1981) and provided the unique sample collection for research. Thanks to V.S. Kamenetsky (School of Physical Sciences, University of Tasmania, Hobart, Australia) for supporting the work on the study of sulfide mineralization of metamorphic rocks at the initial stage and very useful discussions. We wish to thank I.S. Sharygin (Institute of the Earth's Crust SB RAS, Irkutsk) for his help in the selection of the djerfisherite compositions data.

**Conflicts of Interest:** The authors declare no conflict of interest.

## References

1. Reverdatto, V.V. *Facies of Contact Metamorphism*; Nedra: Moscow, Russia, 1970; p. 271.
2. Pertsev, N.N. *High-Temperature Metamorphism and Metasomatism of Carbonate Rocks*; Nauka: Moscow, Russia, 1977.
3. Kerrick, D.M. Contact metamorphism. *Mineral. Soc. Am.* **1991**, *26*, 847.
4. Grapes, R. *Pyrometamorphism*, 2nd ed.; Springer: Berlin/Heidelberg, Germany, 2011; p. 365.
5. Bucher, K.; Grapes, R. *Petrogenesis of Metamorphic Rocks*; Springer: Berlin/Heidelberg, Germany, 2011; p. 428.
6. Gieré, R. Zirconolite, allanite and hoegbomite in a marble skarn from the Bergell contact aureole: Implications for mobility of Ti, Zr and REE. *Contrib. Miner. Pet.* **1986**, *93*, 459–470. [[CrossRef](#)]
7. Spear, F.S.; Pyle, J.M. Apatite, monazite, and xenotime in metamorphic rocks. *Rev. Mineral. Geochem.* **2002**, *48*, 293–335. [[CrossRef](#)]
8. Valley, J.W. Stable isotope thermometry at high temperatures. *Mineral. Soc. Amer.* **2001**, *43*, 365–413.
9. Khoury, H.; Sokol, E.; Clark, I. Calcium uranium oxides from Central Jordan: Mineral assemblages, chemistry, and alteration products. *Can. Min.* **2015**, *53*, 61–82. [[CrossRef](#)]
10. Khoury, H.N.; Sokol, E.V.; Kokh, S.N.; Seryotkin, Y.V.; Nigmatulina, E.N.; Goryainov, S.V.; Belogub, E.V.; Clark, I.D. Tululite, Ca<sub>14</sub>(Fe<sup>3+</sup>, Al)(Al, Zn, Fe<sup>3+</sup>, Si, P, Mn, Mg)<sub>15</sub>O<sub>36</sub>: A new Ca zincate-aluminate from combustion metamorphic marbles, Central Jordan. *Mineral. Petrol.* **2016**, *110*, 125–140. [[CrossRef](#)]
11. Galuskin, E.V.; Gazeev, V.M.; Armbruster, T.; Zadov, A.E.; Galuskina, I.O.; Pertsev, N.N.; Dzierzanowski, P.; Kadiyski, M.; Gurbanov, A.G.; Wrzalik, R.; et al. Lakargiite CaZrO<sub>3</sub>: A new mineral of the perovskite group from the Northern Caucasus, Kabardino-Balkaria, Russia. *Am. Miner.* **2008**, *93*, 1903–1910. [[CrossRef](#)]
12. Galuskina, I.O.; Galuskin, E.V.; Armbruster, T.; Lazic, B.; Kusz, J.; Dzierzanowski, P.; Gazeev, V.M.; Pertsev, N.N.; Prusik, K.; Zadov, A.E.; et al. Elbrusite-(Zr)—A new uranian garnet from the Upper Chegem caldera, Kabardino-Balkaria, Northern Caucasus, Russia. *Am. Mineral.* **2010**, *95*, 1172–1181. [[CrossRef](#)]
13. Galuskin, E.V.; Armbruster, T.; Galuskina, I.O.; Lazic, B.; Winiarski, A.; Gazeev, V.M.; Dzierzanowski, P.; Zadov, A.E.; Pertsev, N.N.; Wrzalik, R.; et al. Vorlanite (CaU<sup>6+</sup>)O<sub>4</sub>—A new mineral from the Upper Chegem caldera, Kabardino-Balkaria, Northern Caucasus, Russia. *Am. Miner.* **2011**, *96*, 188–196. [[CrossRef](#)]
14. Gazeev, V.M.; Gurbanova, O.A.; Zadov, E.A.; Gurbanov, A.G.; Leksin, A.B. Mineralogy of skarn limy xenoliths of Shadil-hoh volcano (Kel volcanic area of the Great Caucasus). *Vestnik Vladikavkazskogo Nauchnogo Tsentra* **2012**, *2*, 23–33.
15. Grew, E.S.; Locock, A.J.; Mills, S.J.; Galuskina, I.O.; Galuskin, E.V.; Hålenius, U. Nomenclature of the garnet supergroup. *Am. Miner.* **2013**, *98*, 785–811. [[CrossRef](#)]
16. Hermann, J.; Rubatto, D.; Korsakov, A.V.; Shatsky, V.S. The age of metamorphism of diamondiferous rocks determined with shrimp dating of zircon. *Russ. Geol. Geophys.* **2006**, *47*, 511–518.
17. Green, T.H.; Hellman, P.L. Fe-Mg partitioning between coexisting garnet and phengite at high pressure, and comments on a garnet-phengite geothermometer. *Lithos* **1982**, *15*, 253–266. [[CrossRef](#)]
18. Hermann, J.; Rubatto, D. Relating zircon and monazite domains to garnet growth zones: Age and duration of granulite facies metamorphism in the Val Malenco lower crust. *J. Metamorph. Geol.* **2003**, *21*, 833–852. [[CrossRef](#)]



19. Watson, E.B.; Wark, D.A.; Thomas, J.B. Crystallization thermometers for zircon and rutile. *Contrib. Miner. Pet.* **2006**, *151*, 413. [[CrossRef](#)]
20. Tomkins, H.S.; Powell, R.; Ellis, D.J. The pressure dependence of the zirconium-in-rutile thermometer. *J. Metamorph. Geol.* **2007**, *25*, 703–713. [[CrossRef](#)]
21. Parat, F.; Dungan, M.A.; Streck, M.J. Anhydrite, pyrrhotite, and sulfurrichapatite: Tracing the sulfur evolution of an Oligocene andesite (Eagle Mountain, CO, USA). *Lithos* **2002**, *64*, 63–75. [[CrossRef](#)]
22. Britvin, S.N.; Bogdanova, A.N.; Boldyreva, M.M.; Aksenova, G.Y. Rudashevskyite, the Fe-dominant analogue of sphalerite, a new mineral: Description and crystal structure. *Am. Miner.* **2008**, *93*, 902–909. [[CrossRef](#)]
23. Marks, M.A.W.; Wenzel, T.; Whitehouse, M.J.; Loose, M.; Zack, T.; Barth, M.; Worgard, L.; Krasz, V.; Eby, G.N.; Stosnach, H.; et al. The volatile inventory (F, Cl, Br, S, C) of magmatic apatite: An integrated analytical approach. *Chem. Geol.* **2012**, *291*, 241–255. [[CrossRef](#)]
24. Barton, P.B. Sulfide petrology. *Mineral. Soc. Am. Rev. Mineral.* **1974**, *1*, B1–B11.
25. Slotznick, S.P.; Eiler, J.M.; Fischer, W.W. The effects of metamorphism on iron mineralogy and the iron speciation redox proxy. *Geochim. Cosmochim. Acta.* **2018**, *224*, 96–115. [[CrossRef](#)]
26. Vaughan, D.J. Sulfide mineralogy and geochemistry. *Mineral. Soc. Amer.* **2006**, *61*, 714.
27. Brown, J.L.; Christy, A.G.; Ellis, D.J.; Arculus, R.J. Prograde sulfide metamorphism in blueschist and eclogite, New Caledonia. *J. Pet.* **2014**, *55*, 643–670. [[CrossRef](#)]
28. Robert, R. Seal II. Sulfur isotope geochemistry of sulfide minerals. *Rev. Mineral. Geochem.* **2006**, *61*, 633–677.
29. Reverdatto, V.V. High-temperature contact metamorphism of limestones in the Podkamennaya Tunguska basin. *Dokl. Earth Sci. USSR.* **1964**, *155*, 104–107.
30. Sokol, E.V.; Polyansky, O.P.; Semenov, A.N.; Reverdatto, V.V.; Kokh, S.N.; Devyatyyarova, A.S.; Kolobov, V.Y.; Khvorov, P.V.; Babichev, A.V. High-grade contact metamorphism in the Kochumdek River valley (Podkamennaya Tunguska basin, East Siberia): Evidence for magma flow. *Russ. Geol. Geophys.* **2019**, *60*, 386–399.
31. Devyatyyarova, A.S. Potassium Sulfides in Spurrite Marbles from the Kochumdek River. In Proceedings of the 55 International Scientific Student Conference, Novosibirsk, Russia, 17–20 April 2017; p. 88.
32. Devyatyyarova, A.S. Specific Sulfide Mineralization in Spurrite Marbles from the Kochumdek Contact Aureole (Podkamennaya Tunguska basin). In Proceedings of the XXIIIrd Scientific Youth School “Metallogeny of Ancient and Modern Oceans–2017. Differentiation and Reasons of Diversity of Ore Deposits”, Miass, Russia, 24–28 April 2017; pp. 229–232.
33. Golovin, A.V.; Goryainov, S.V.; Kokh, S.N.; Sharygin, I.S.; Rashchenko, S.V.; Kokh, K.A.; Devyatyyarova, A.S.; Sokol, E.V. The application of raman spectroscopy to djerfisherite identification. *J. Raman Spectrosc.* **2017**, *48*, 1574–1582. [[CrossRef](#)]
34. Sokol, E.V.; Devyatyyarova, A.S.; Kokh, S.N.; Reverdatto, V.V.; Artemyev, D.A.; Kolobov, V.Y. Sulfide mineralization hosted by spurrite-mervinite marbles (Kochumdek River, East Siberia). *Dokl. Earth Sci.* **2019**, *489*, 1326–1329. [[CrossRef](#)]
35. Devyatyyarova, A.S.; Artemyev, D.A.; Abersteiner, A.; Sokol, E.V. Isotope-Geochemical Characteristics of Sulfides in Spurrite Marbles from the Kochumdek River (Podkamennaya Tunguska basin). In Proceedings of the Professor, V.V. Zaykov XXVIth Scientific Youth School “Metallogeny of Ancient and Modern Oceans–2020. Critical Metals in Ore-Forming Systems”, Miass, Russia, 22 April 2020; pp. 205–209.
36. Malich, N.S.; Grigoriev, V.V. Correlation of Magmatism and Tectonics in the lower Podkamennaya Tunguska and Bakhta River Basins. In *Geology and Mineral Resources in the Siberian Craton*; VSEGEI: Leningrad, Russia, 1960; pp. 27–36.
37. Vasil’ev, Y.R.; Zolotukhin, V.V.; Feoktistov, G.D.; Prusskaya, S.N. Evaluation of the volumes and genesis of Permo-Triassic trap magmatism on the Siberian platform. *Russ. Geol. Geophys.* **2000**, *41*, 1696–1705.
38. Dobretsov, N.L.; Kirdyashkin, A.A.; Kirdyashkin, A.G.; Vernikovskiy, V.A.; Gladkov, I.N. Modelling of thermochemical plumes and implications for the origin of the Siberian traps. *Lithos* **2008**, *100*, 66–92. [[CrossRef](#)]
39. Dobretsov, N.L. 250 Ma large igneous provinces of Asia: Siberian and emeishan traps (plateau basalts) and associated granitoids. *Russ. Geol. Geophys.* **2005**, *9*, 847–868.
40. Zolotukhin, V.V.; Al’ mukhamedov, A.I. Basalts of the Siberian platform: Distribution, Mineral Composition, and Mechanism of Formation. In *Traps of Siberia and Deccan: Similarities and Differences*; Polyakov, G.V., Ed.; Nauka: Novosibirsk, Russia, 1991; pp. 7–39.
41. Prusskaya, S.N. *Petrology of Intrusive Trappean Magmatism in the Western Siberian Craton: Evidence from Petroleum Drilling*; Siberian Federal University: Krasnoyarsk, Russia, 2008; p. 248.
42. Egorova, V.; Latypov, R. Mafic–ultramafic sills: New insights from M- and S-shaped mineral and whole-rock compositional profiles. *J. Pet.* **2013**, *54*, 2155–2191. [[CrossRef](#)]
43. Poryadin, V.S.; Strunin, B.M.; Turchin, A.V.; Komarov, V.V.; Fainer, Y.B. *State Geological Map of the USSR, Scale 1:200,000, Ser. Turukhansk, Sheet R-46-XIV. Explanatory Note*; Krasnoyarskoe Territorialnoe Geologicheskoe Upravlenie: Moscow, Russia, 1977.
44. Alekseenko, V.D.; Alasev, V.A.; Barmin, V.A.; Belolipetskaya, L.I.; Bozhko, V.V.; Varganov, A.S.; Egorov, V.N.; Egorov, A.S.; Kazhaeva, O.D.; Kachevsky, L.K.; et al. State geological Map of the Russian Federation, scale 1:1,000,000 (third generation). In *Ser. Angara-Yenisei. Sheet R-46-North Yenisei. Explanatory Note Kart*; VSEGEI: St. Petersburg, Russia, 2010.
45. Sobolev, V.S. *Selected Works. Trap Petrology*; Nauka: Novosibirsk, Russia, 1986; p. 210.
46. Reverdatto, V.V. Metamorphism in the contacts of Anakit trappean massif in the Low Tunguska River. In *Materials on Genetik and Experimental Mineralogy*; Transactions of the Institute of Geology and Geophysics Siberian Branch Academy of Sciences of USSR: Novosibirsk, Russian, 1964; pp. 97–168.

47. Pertsev, N.N.; Shmulovich, K.I. Physicochemical conditions of larnite-merwinite facies contact metamorphism: A case study from the Podkamennaya Tunguska basin. *Izvestiya AN SSSR* **1972**, *6*, 39–47.
48. Tesakov, Y.I. New silurian formations in the southwest of the Siberian platform. *Novosti paleontologii i stratigrafii. Suppl. Russ. Geol. Geophys.* **2009**, *12*, 29–41.
49. Heinrich, W.; Gottschalk, M. Fluid flow patterns and infiltration isograds in melilite marbles from the Bufa del Diente contact metamorphic aureole, north-east Mexico. *J. Metamorph. Geol.* **1994**, *12*, 345–359. [[CrossRef](#)]
50. Shatsky, V.; Sitnikova, E.; Kozmenko, O.; Palessky, S.; Nikolaeva, I.; Zayachkovsky, A. Behavior of incompatible elements during ultrahigh-pressure metamorphism (by the example of rocks of the Kokchetav massif). *Russ. Geol. Geophys.* **2006**, *47*, 482–496.
51. Element, C.A.S. Method 3051A-microwave assisted acid digestion of sediments, sludges, soils, and oils. *Z. Anal. Chem.* **2007**, *111*, 362–366.
52. Carvalho, L.; Monteiro, R.; Figueira, P.; Mieiro, C.; Almeida, J.; Pereira, E.; Magalhães, V.; Pinheiro, L.; Vale, C. Vertical distribution of major, minor and trace elements in sediments from mud volcanoes of the Gulf of Cadiz: Evidence of Cd, As and Ba fronts in upper layers. *Deep Sea Res. Part. I Oceanogr. Res. Pap.* **2018**, *131*, 133–143. [[CrossRef](#)]
53. Sokol, E.V.; Kokh, S.N.; Seryotkin, Y.V.; Deviatiiarova, A.S.; Goryainov, S.V.; Sharygin, V.V.; Khoury, H.N.; Karmanov, N.S.; Danilovsky, V.A.; Artemyev, D.A.; et al. Ultrahigh-temperature sphalerite from Zn-Cd-Se-rich combustion metamorphic marbles, Daba Complex, Central Jordan: Paragenesis, chemistry, and structure. *Minerals* **2020**, *10*, 822. [[CrossRef](#)]
54. Artemyev, D.A.; Ankushev, M.N. Trace elements of Cu-(Fe)-sulfide inclusions in bronze age copper slags from South Urals and Kazakhstan: Ore sources and alloying additions. *Minerals* **2019**, *9*, 746. [[CrossRef](#)]
55. Humphries, D.W. The Preparation of thin Sections of Rocks, Minerals and Ceramics. In *Royal Microscopical Society Microscopy Handbooks*; Oxford University Press: Oxford, UK, 1992.
56. Longerich, H.P.; Jackson, S.E.; Günther, D. Inter-laboratory note. Laser ablation inductively coupled plasma mass spectrometric transient signal data acquisition and analyte concentration calculation. *J. Anal. At. Spectrom.* **1996**, *11*, 899–904. [[CrossRef](#)]
57. Wilson, S.A.; Ridley, W.I.; Koenig, A.E. Development of sulphide calibration standards for the laser ablation inductively-coupled plasma mass spectrometry technique. *J. Anal. Spectrom.* **2002**, *17*, 406–409. [[CrossRef](#)]
58. Paton, C.; Hellstrom, J.; Paul, B.; Woodhead, J.; Hergt, J. Iolite: Freeware for the visualisation and processing of mass spectrometric data. *J. Anal. At. Spectrom.* **2011**, *26*, 2508–2518. [[CrossRef](#)]
59. Canberra Industries Inc. *Model S506 Interactive Peak Fit. User's Manual*; Canberra Industries Inc.: Canberra, NSW, Australia, 2002.
60. Gao, S.; Luo, T.C.; Zhang, B.R.; Zhang, H.F.; Han, Y.W.; Hu, Y.K.; Zhao, Z.D. Chemical composition of the continental crust as revealed by studies in east China. *Geochim. Cosmochim. Acta.* **1998**, *62*, 1959–1975. [[CrossRef](#)]
61. Deviatiiarova, A.S. Crystal-Chemical Element Fractionation Under HT-LP Metamorphic Conditions: Case Study from Kochumdek Contact Aureole (Podkamennaya Tunguska basin). In *Proceedings of the XIX International Meeting on Crystal Chemistry, X-ray Diffraction and Spectroscopy of Minerals, Apatity, Russia, 2–9 July 2019*; p. 213.
62. Gerasimova, Y.V.; Oreshonkov, A.S.; Romanova, O.B.; Ivanenko, A.A.; Krylov, A.S. Raman and infrared characterization of gadolinium-doped manganese sulfide. *Spectrosc. Lett.* **2017**, *50*, 55–58. [[CrossRef](#)]
63. Scocioreanu, M.; Baibarac, M.; Baltog, I.; Pasuk, I.; Velula, T. Photoluminescence and raman evidence for mechanico-chemical interaction of polyaniline-emeraldine base with ZnS in cubic and hexagonal phase. *J. Solid. State. Chem.* **2012**, *186*, 217–223. [[CrossRef](#)]
64. Osadchii, E.G.; Gorbaty, Y.E. Raman spectra and unit cell parameters of sphalerite solid solutions (Fe<sub>x</sub>Zn<sub>1-x</sub>S). *Geochim. Cosmochim. Acta.* **2010**, *74*, 568–573. [[CrossRef](#)]
65. Makovicky, E. Crystal structures of sulfides and other chalcogenides. *Rev. Mineral. Geochem.* **2006**, *61*, 7–125. [[CrossRef](#)]
66. Barkov, A.Y.; Martin, R.F.; Cabri, L.J. Rare sulfides enriched in K, Tl and Pb from the Noril'sk and Salmagorsky complexes, Russia: New data and implications. *Min. Mag.* **2015**, *79*, 799–808. [[CrossRef](#)]
67. Dobrovol'skaya, M.G. *Alkaline Metals Sulfides in the Nature*; Nauka: Moscow, Russia, 2018.
68. Li, C.; Ripley, E.M.; Naldrett, A.J. Compositional variations of olivine and sulfur isotopes in the Noril'sk and Talnakh intrusions, Siberia: Implications for ore-forming processes in dynamic magma conduits. *Econ. Geol.* **2003**, *98*, 69–86. [[CrossRef](#)]
69. Jamtveit, B.; Dahlgren, S.; Austrheim, H. High-grade contact metamorphism of calcareous rocks from the Oslo Rift, Southern Norway. *Am. Miner.* **1997**, *82*, 1241–1254. [[CrossRef](#)]
70. Chakhmouradian, A.R.; Mitchell, R.H.; Horvath, L. Rb–Cs-enriched rasvumite and sectorial loparite–lueshite intergrowths from the Mont Saint-Hilaire alkaline complex, Quebec, Canada. *Geol. Assoc. Can. Mineral. Assoc. Can. Program Abstr.* **2001**, *26*, 24.
71. Chakhmouradian, A.R.; Halden, N.M.; Mitchell, R.H.; Horváth, L. Rb–Cs-rich rasvumite and sector-zoned “loparite-(Ce)” from Mont Saint-Hilaire (Québec, Canada) and their petrologic significance. *Eur. J. Mineral.* **2007**, *19*, 533–546. [[CrossRef](#)]
72. Sharygin, V.V.; Kamenetsky, V.S.; Kamenetsky, M.B. Potassium sulfides in kimberlite-hosted chloride-«nyerereite» and chloride clasts of Udachnaya-East pipe, Yakutia, Russia. *Can. Miner.* **2008**, *46*, 1076–1095. [[CrossRef](#)]
73. Dobrovol'skaya, M.G.; Tsepina, A.I.; Ilupin, I.P.; Ponomarenko, A.I. *Djerfisherite from Yakutia Kimberlites Minerals and Parageneses of Endogenic Deposits*; Nauka: Leningrad, Russia, 1975.
74. Clarke, D.B. Synthesis of Nickeloan Djerfisherites and the Origin of Potassic Sulphides at the Frank Smith mine. In *The Mantle Sample: Inclusions in Kimberlites and Other Volcanics*; Broyd, F.R., Meyer, H.O.A., Eds.; American Geophysical Union: Washington, DC, USA, 1979; Volume 16, pp. 300–308.

75. Distler, V.V.; Ilupin, I.P.; Laputina, I.P. Sulfides of deep-seated origin in kimberlites and some aspects of copper-nickel mineralization. *Int. Geol. Rev.* **1987**, *29*, 456–464. [[CrossRef](#)]
76. Spetsius, Z.V.; Bulanova, G.P.; Leskova, N.V. Djerfisherite and its genesis in kimberlitic rocks. *Dokl. Acad. Sci. USSR* **1987**, *293*, 199–202.
77. Bulanova, G.P.; Spetsius, Z.V.; Leskova, N.V. *Sulphides in Diamonds and Xenoliths from Yakutian Kimberlite Pipes*; Nauka: Novosibirsk, Russia, 1990; p. 120.
78. Sharygin, V.V.; Golovin, A.V.; Pokhilenko, N.P.; Kamenetsky, V.S. Djerfisherite in the Udachnaya-East pipe kimberlites (Sakha-Yakutia, Russia): Paragenesis, composition and origin. *Eur. J. Mineral.* **2007**, *19*, 51–63. [[CrossRef](#)]
79. Sharygin, I.S.; Golovin, A.V.; Pokhilenko, N.P. Djerfisherite in xenoliths of sheared peridotite in the Udachnaya-East pipe (Yakutia): Origin and relationship with kimberlite magmatism. *Russ. Geol. Geophys.* **2012**, *53*, 247–261. [[CrossRef](#)]
80. Abersteiner, A.; Kamenetsky, V.S.; Goemann, K.; Golovin, A.V.; Sharygin, I.S.; Giuliani, A.; Rodemann, T.; Spetsius, Z.V.; Kamenetsky, M. Djerfisherite in kimberlites and their xenoliths: Implications for kimberlite melt evolution. *Contrib. Mineral. Petrol.* **2019**, *174*, 8. [[CrossRef](#)]
81. Sharygin, I.S.; Golovin, A.V.; Pokhilenko, N.P. Djerfisherite in kimberlites of the Kuoikskoe field as an indicator of enrichment of kimberlite melts in chlorine. *Dokl. Earth Sci.* **2011**, *436*, 301–307. [[CrossRef](#)]
82. Henderson, C.M.B.; Kogarko, L.N.; Plant, D. Extreme closed system fractionation of volatile-rich, ultrabasic peralkaline melt inclusions and the occurrence of djerfisherite in the Kugda alkaline complex, Siberia. *Min. Mag.* **1999**, *63*, 433–438. [[CrossRef](#)]
83. Zaccarini, F.; Thalhhammer, O.A.R.; Princivale, F.; Lenaz, D.; Stanley, C.J.; Garuti, G. Djerfisherite in the guli dunite complex, polar Siberia: A primary or metasomatic phase. *Can. Min.* **2007**, *45*, 1201–1211. [[CrossRef](#)]
84. Clay, P.L.; O'Driscoll, B.; Upton, B.G.J.; Busemann, H. Characteristics of djerfisherite from fluid-rich, metasomatized alkaline intrusive environments and anhydrous enstatite chondrites and achondrites. *Am. Miner.* **2014**, *99*, 1683–1693. [[CrossRef](#)]
85. Takechi, Y.; Kusachi, I.; Nakamuta, Y.; Kase, K. Nickel-bearing djerfisherite in gehlenite-spurrite skarn at Kushiro, Hiroshima prefecture, Japan. *Resour. Geol.* **2000**, *50*, 179–184. [[CrossRef](#)]
86. Fuchs, L.H. Djerfisherite, alkali copper-iron sulfide: A new mineral from enstatite chondrites. *Science* **1966**, *153*, 166–167. [[CrossRef](#)] [[PubMed](#)]
87. Lin, Y.; El Goresy, A. A comparative study of opaque phases in Qingzhen (EH3) and MacAlpine Hills 88136 (EL3): Representatives of EH and EL parent bodies. *Meteorit. Planet. Sci.* **2002**, *37*, 577–599. [[CrossRef](#)]
88. Faure, G. *Principles of Isotope Geology*, 2nd ed.; John Wiley and Sons: New York, NY, USA, 1986; 589p.
89. Rickard, D. *Sulfidic Sediments and Sedimentary Rocks*; Elsevier: Amsterdam, The Netherlands, 2012.
90. Claypool, G.E.; Holser, W.T.; Kaplan, I.R.; Sakai, H.; Zak, I. The age curves of sulfur and oxygen isotopes in marine sulfate and their mutual interpretation. *Chem. Geol.* **1980**, *28*, 199–260. [[CrossRef](#)]
91. Buchko, I.V.; Sorokin, A.A.; Ponomarchuk, V.A.; Izokh, A.E. Geochemical features and geodynamic setting of formation of the Lukinda dunite-troctolite-gabbro massif (southeastern framing of the Siberian Platform). *Russ. Geol. Geophys.* **2012**, *53*, 636–648. [[CrossRef](#)]
92. Pokrovsky, B.G.; Zaitsev, A.V.; Dronov, A.V.; Bujakaite, M.I.; Petrov, O.L.; Timokhin, A.V. C, O, S, and Sr isotope geochemistry and chemostratigraphy of Ordovician sediments in the Moyero River section, northern Siberian platform. *Lithol. Min. Res.* **2018**, *53*, 283–306. [[CrossRef](#)]
93. Ripley, E.M.; Lightfoot, P.C.; Li, C.; Elswick, E.R. Sulfur isotopic studies of continental flood basalts in the Noril'sk region: Implications for the association between lavas and ore-bearing intrusions. *Geochim. Cosmochim. Acta.* **2003**, *67*, 2805–2817. [[CrossRef](#)]
94. Morse, J.W.; Luther Iii, G.W. Chemical influences on trace metal-sulfide interactions in anoxic sediments. *Geochim. Cosmochim. Acta.* **1999**, *63*, 3373–3378. [[CrossRef](#)]
95. Large, R.R.; Halpin, J.A.; Danyushevsky, L.V.; Maslennikov, V.V.; Bull, S.W.; Long, J.A.; Gregory, D.D.; Lounejeva, E.; Lyons, T.W.; Sack, P.J.; et al. Trace element content of sedimentary pyrite as a new proxy for deep-time ocean-atmosphere evolution. *Earth Planet. Sci. Lett.* **2014**, *389*, 209–220. [[CrossRef](#)]
96. Parnell, J.; Perez, M.; Armstrong, J.; Bullock, L.; Feldmann, J.; Boyce, A.J. Geochemistry and metallogeny of neoproterozoic pyrite in oxic and anoxic sediments. *Geochem. Perspect. Lett.* **2018**, *7*, 12–16. [[CrossRef](#)]
97. Vernon, R.H.; White, R.W.; Clarke, G.L. False metamorphic events inferred from misinterpretation of microstructural evidence and P-T data. *J. Metamorph. Geol.* **2008**, *26*, 437–449. [[CrossRef](#)]
98. Itaya, T.; Brothers, R.N.; Black, P.M. Sulfides, oxides and sphene in high-pressure schists from New Caledonia. *Contrib. Miner. Pet.* **1985**, *91*, 151–162. [[CrossRef](#)]
99. Kawakami, T.; Ellis, D.J.; Christy, A.G. Sulfide evolution in high-temperature to ultrahigh-temperature metamorphic rocks from Lutzow-Holm complex, East Antarctica. *Lithos* **2006**, *92*, 431–446. [[CrossRef](#)]
100. Seryotkin, Y.V.; Sokol, E.V.; Kokh, S.N. Natural pseudowollastonite: Crystal structure, associated minerals, and geological context. *Lithos* **2012**, *134*, 75–90. [[CrossRef](#)]
101. Tomashyk, V.; Feychuk, P.; Scherbak, L. *Ternary Alloys Based on II-VI Semiconductor Compounds*; 1st ed.; CRC Press: Boca Raton, FL, USA, 2013; p. 560.
102. Knitter, S.; Binnewies, M. Chemical transport of MnS/ZnS, FeS/ZnS, and FeS/MnS mixed crystals. *J. Inorg. Gen. Chem.* **1999**, *625*, 1582–1588.

103. Knitter, S.; Binnewies, M. Chemical vapor transport of solid solutions. 7. Chemical vapor transport of FeS/MnS/ZnS mixed crystals. *J. Inorg. Gen. Chem.* **2000**, *626*, 2335–2339.
104. Gorbachev, N.S.; Nekrasov, I.Y. Genesis of synthetic and natural potassium sulfides. *Dokl. Acad. Sci. USSR.* **1980**, *251*, 126–129.
105. Osadchii, V.O.; Voronin, M.V.; Baranov, A.V. Mineralogy of Potassium-Iron Sulfides and Phase Relations in the System K-Fe-S-(Cl). In Proceedings of the XXVII All-Russian Youth Conference with the Participation of Researchers from other Countries, Irkutsk, Russian, 22–28 May 2017; pp. 166–167.
106. Osadchii, V.O.; Voronin, M.V.; Baranov, A.V. Phase equilibria in the  $KFe_2S_2$ -Fe-S system at 300–600 °C and bartonite stability. *Contrib. Miner. Pet.* **2018**, *173*, 44. [[CrossRef](#)]
107. Mitchell, R.H. Crystal structures of  $CsFe_2S_3$  and  $RbFe_2S_3$ : Synthetic analogs of rasvumite  $KFe_2S_3$ . *J. Solid. State. Chem.* **2004**, *177*, 1867–1872. [[CrossRef](#)]
108. Amthauer, G.; Bente, K. Mixed-valent iron in synthetic rasvumite,  $KFe_2S_3$ . *Naturwissenschaften* **1983**, *70*, 146–147. [[CrossRef](#)]
109. Boller, H. On the synthesis, crystal chemistry and magnetic properties of rasvumite and related compounds. *Acta Cryst.* **2004**, *60*, s47. [[CrossRef](#)]
110. Voronin, M.V.; Osadchii, V.O.; Baranov, A.V. Phase Relations Involving Chlorbartonite in the K-Fe-S-Cl System. In Proceedings of the International Conference on Geochemistry and Related Subjects “Goldschmidt”, Barcelona, Spain, 18–23 August 2019; p. 3535.
111. Buick, I.S.; Cartwright, I. Stable isotope constraints on the mechanism of fluid flow during contact metamorphism around the Marulan Batholith, NSW, Australia. *J. Geochem. Explor.* **2000**, *69*, 291–295. [[CrossRef](#)]
112. Barkov, A.Y.; Laajoki, K.V.O.; Gehor, S.A.; Yakovlev, Y.N.; Taikina-Aho, O. Chlorine-poor analogues of djerfisherite-thalfenisite from Noril’sk, Siberia, and Salmagorsky, Kola Peninsula, Russia. *Can. Miner.* **1997**, *35*, 1421–1430.
113. Sluzhenikin, S.F.; Laputina, I.P. Composition of Minerals of the Djerfisherite Group in Copper-Nickel Ores of the Talnakh Deposit. In Proceedings of the “Microprobe and Progress in Geology”, Suzdal, Russia, 21–28 April 1989; pp. 107–110.
114. Sharygin, V.V.; Starikova, A.Y. Sulfide Associations in Garnet-Melilite-wollastonite Skarns of the Tazheran Alkaline Massif, Baikal Region. In Proceedings of the XXVII International Conference School “Geochemistry of Alkaline Rocks”, Moscow-Koktebel, Russia, 9–16 September 2010; pp. 164–166.
115. Starikova, A.E. Mineralogy of Metasomatic Rocks of the Tazheran Massif (Western Baikal Area). Ph.D. Thesis, Institute of Geology and Mineralogy SB RAS, Novosibirsk, Russia, 21 May 2013; p. 207.
116. Heinrich, W.; Churakov, S.S.; Gottschalk, M. Mineral-fluid equilibria in the system  $CaO$ - $MgO$ - $SiO_2$ - $H_2O$ - $CO_2$ - $NaCl$  and the record of reactive fluid flow in contact metamorphic aureoles. *Contrib. Miner. Pet.* **2004**, *148*, 131–149. [[CrossRef](#)]